



**HAL**  
open science

## Empirical determination of the shape of dust attenuation curves in star-forming galaxies

Vivienne Wild, Stéphane Charlot, Jarle Brinchmann, Timothy Heckman,  
Oliver Vince, Camilla Pacifici, Jacopo Chevallard

### ► To cite this version:

Vivienne Wild, Stéphane Charlot, Jarle Brinchmann, Timothy Heckman, Oliver Vince, et al.. Empirical determination of the shape of dust attenuation curves in star-forming galaxies. *Monthly Notices of the Royal Astronomical Society*, 2011, 417, pp.1760-1786. 10.1111/j.1365-2966.2011.19367.x . insu-03645851

**HAL Id: insu-03645851**

**<https://insu.hal.science/insu-03645851>**

Submitted on 22 Apr 2022

**HAL** is a multi-disciplinary open access archive for the deposit and dissemination of scientific research documents, whether they are published or not. The documents may come from teaching and research institutions in France or abroad, or from public or private research centers.

L'archive ouverte pluridisciplinaire **HAL**, est destinée au dépôt et à la diffusion de documents scientifiques de niveau recherche, publiés ou non, émanant des établissements d'enseignement et de recherche français ou étrangers, des laboratoires publics ou privés.

# Empirical determination of the shape of dust attenuation curves in star-forming galaxies

Vivienne Wild,<sup>1,2\*</sup> Stéphane Charlot,<sup>1</sup> Jarle Brinchmann,<sup>3,4</sup> Timothy Heckman,<sup>5</sup>  
Oliver Vince,<sup>1,6</sup> Camilla Pacifici<sup>1</sup> and Jacopo Chevallard<sup>1</sup>

<sup>1</sup>*Institut d'Astrophysique de Paris, CNRS, Université Pierre & Marie Curie, UMR 7095, 98bis bd Arago, 75014 Paris, France*

<sup>2</sup>*Institute for Astronomy, University of Edinburgh, Royal Observatory, Blackford Hill, Edinburgh EH9 3HJ (SUPA)*

<sup>3</sup>*Leiden Observatory, Leiden University, 2300RA, Leiden, the Netherlands*

<sup>4</sup>*Centro de Astrofísica, Universidade do Porto, Rua das Estrelas, 4150-762 Porto, Portugal*

<sup>5</sup>*Department of Physics and Astronomy, The Johns Hopkins University, 3400 N. Charles Street, Baltimore, MD 21218, USA*

<sup>6</sup>*Astronomical Observatory of Belgrade, Volgina 7, 11060 Belgrade, Serbia*

Accepted 2011 July 1. Received 2011 June 28; in original form 2011 February 2

## ABSTRACT

We present a systematic study of the shape of the dust attenuation curve in star-forming galaxies from the far-ultraviolet (far-UV) to the near-infrared (NIR;  $\sim 0.15\text{--}2\ \mu\text{m}$ ), as a function of specific star formation rate ( $\psi_S$ ) and axial ratio ( $b/a$ ), for galaxies with and without a significant bulge. Our sample comprises 23 000 (15 000) galaxies with a median redshift of 0.07, with photometric entries in the Sloan Digital Sky Survey (SDSS), UKIRT Infrared Deep Sky Survey–Large Area Survey and *Galaxy Evolution Explorer*–All-Sky Imaging Survey catalogues and emission-line measurements from the SDSS spectroscopic survey. We develop a new pair-matching technique to isolate the dust attenuation curves from the stellar continuum emission. The main results are: (i) the slope of the attenuation curve in the optical varies weakly with  $\psi_S$ , strongly with  $b/a$ , and is significantly steeper than the Milky Way extinction law in bulge-dominated galaxies; (ii) the NIR slope is constant and matches the slope of the Milky Way extinction law; (iii) the UV has a slope change consistent with a dust bump at  $2175\ \text{\AA}$  which is evident in all samples and varies strongly in strength with  $b/a$  in the bulge-dominated sample; (iv) there is a strong increase in emission-line-to-continuum dust attenuation ( $\tau_{V,\text{line}}/\tau_{V,\text{cont}}$ ) with both decreasing  $\psi_S$  and increasing  $b/a$ ; and (v) radial gradients in dust attenuation increase strongly with increasing  $\psi_S$ , and the presence of a bulge does not alter the strength of the gradients. These results are consistent with the picture in which young stars are surrounded by dense ‘birth clouds’ with low covering factor which disperse on time-scales of  $\sim 10^7$  yr and the diffuse interstellar dust is distributed in a centrally concentrated disc with a smaller scaleheight than the older stars that contribute the majority of the red and NIR light. Within this model, the path-length of diffuse dust, but not of birth-cloud dust, increases with increasing inclination and the apparent optical attenuation curve is steepened by the differential effect of larger dust opacity towards younger stars than towards older stars. Additionally, our findings suggest that: (i) galaxies with higher star formation rates per unit stellar mass have a higher fraction of diffuse dust, which is more centrally concentrated; (ii) the observed strength of the  $2175\text{-\AA}$  dust feature is affected predominantly by global geometry; and (iii) only highly inclined discs are optically thick. We provide new empirically derived attenuation curves for correcting the light from star-forming galaxies for dust attenuation.

**Key words:** dust, extinction – galaxies: fundamental parameters – galaxies: ISM.

## 1 INTRODUCTION

Dust is a ubiquitous component of the baryonic Universe, potentially condensing out of the interstellar medium as soon as the first generation of stars have expired and provided the requisite metals

\*E-mail: vw@roe.ac.uk

(Meurer et al. 1997; Hughes et al. 1998; Bertoldi et al. 2003; Draine 2009). The presence of dust in galaxies hampers our measurements of intrinsic galaxy properties, including stellar masses and star formation rate (SFR), when observations are limited in wavelength coverage or availability of spectroscopic data (Calzetti et al. 2007). It also impacts our measurements of global population statistics, such as luminosity functions and colour–magnitude diagrams. The strong systematic variation of dust content with stellar mass, SFR and morphology can lead to significant biases in results if not correctly accounted for (Brinchmann et al. 2004; Driver et al. 2007; Maller et al. 2009; da Cunha et al. 2010; Gilbank et al. 2010). For example, unphysical correlations between estimated stellar masses and inclinations can indicate an incorrect treatment of dust (Maller et al. 2009), and luminosity, mass and SFR densities are found to be higher when the larger dust attenuations in the discs of star-forming galaxies are accounted for (Brinchmann et al. 2004; Driver et al. 2007). Dust expelled from galaxies and residing in galaxy haloes (Wild & Hewett 2005; Hewett & Wild 2007) can even have implications for the estimation of cosmological parameters (Ménard, Kilbinger & Scranton 2010).

For several decades, research into dust in galaxies focused around the question of whether spiral discs are optically thick or thin. By studying large samples of galaxies with varying inclinations to the line of sight, in combination with models for the dust distribution in galaxies, near-infrared (NIR) photometry, or rotation curves, the amount of attenuation suffered by starlight before it reaches the observer can be constrained (e.g. Giovanelli & Haynes 2002; Masters, Giovanelli & Haynes 2003; Driver et al. 2007; Maller et al. 2009; Masters et al. 2010; Yip et al. 2010). The consensus is that the stellar continua in galaxy discs suffer 0–1 mag of attenuation in the  $B$  band [or Sloan Digital Sky Survey (SDSS)  $g$  band], depending on inclination. Galaxy bulges may well suffer greater attenuation due to radial gradients in dust discs. Driver et al. (2007) find inclination-dependent attenuations in bulges of 0.8–2.6 mag in the  $B$  band.

While the extinction<sup>1</sup> of starlight by dust can be measured with relative ease along lines of sight to stars in the Milky Way (MW) and closest galaxies (Small Magellanic Cloud and Large Magellanic Cloud, hereinafter SMC and LMC, respectively), the integration of light over the entire stellar population of a distant galaxy introduces considerable complications. First, the dust is not distributed uniformly throughout the galaxy: there are dense birth clouds around the youngest stars, there is a diffuse component exhibiting strong radial gradients (e.g. Persson & Helou 1987; Peletier et al. 1995; Boissier et al. 2004; Muñoz-Mateos et al. 2009), and there is some evidence that diffuse interstellar dust is distributed throughout the disc with a smaller scaleheight than that of the stars (Xilouris et al. 1999). Secondly, the dust does not approximate a uniform screen in front of the stars: dust and stars are mixed, potentially causing an additional scattering component which can affect the shape of the attenuation curve relative to the underlying extinction curve. Indeed, Boquien et al. (2009) suggest that variation in extinction laws and dust–star geometry may cause the scatter in the dust attenuation versus reddening (e.g.  $IRX-\beta$ ) relation observed in star-forming galaxies, and Buat et al. (2011) find tentative evidence for a steeper

dust attenuation curve in ordinary star-forming galaxies than found in starburst galaxies by Calzetti et al. (2000, hereinafter C00).

On the other hand, the sensitivity of the shape of the dust attenuation curve to dust grain properties and dust–star geometry allows us to extract information on the properties and distribution of dust in galaxies. For example, a flatter blue/ultraviolet (blue/UV) attenuation curve is generally expected in the case of spatially mixed dust and stars, as the least extinguished stars contribute a greater fraction of the total emergent blue light than red light (e.g. Gordon, Calzetti & Witt 1997; Charlot & Fall 2000). Dust features, the strongest one being at 2175 Å, can provide further constraints. Models suggest that the 2175-Å feature should vary in strength in galaxy spectral energy distributions (SEDs), depending upon the properties and geometry of the dust (Granato et al. 2000; Witt & Gordon 2000). Observationally, there is some evidence for a 2175-Å absorption feature in local star-forming galaxies (Conroy, Schiminovich & Blanton 2010) and high-redshift galaxies (Noll et al. 2009), but clear absence in local starburst galaxies (Calzetti, Kinney & Storchi-Bergmann 1994) and the SMC (Pei 1992; Gordon et al. 2003).

In this paper, we measure empirically the optical–NIR and UV-to-NIR attenuation curves, using a sample of  $\sim 23\,000$  and  $\sim 15\,000$  star-forming galaxies, respectively, as a function of radius, specific SFR ( $\psi_S \equiv \text{SFR}/M^*$ ) and inclination angle ( $b/a$ ), for galaxies both with and without massive bulges. We achieve this by carefully pair-matching galaxies to remove unwanted stellar population signal. Spectroscopic information provides a measure of relative dust content via the Balmer emission lines, allowing us to combine galaxy pairs in such a way as to reveal an average attenuation curve with very high signal-to-noise ratio (S/N).

The development of this new, robust, statistical method to measure dust attenuation curves in galaxies with a range of different underlying stellar populations allows us for the first time to observe trends in the shape of the attenuation curve as a function of galaxy properties. Deriving attenuation curves using different-sized apertures enables us to measure the strong radial gradients in dust opacity with  $\psi_S$ . We compare dust opacity suffered by emission lines to that suffered by the optical continuum, finding strong trends with  $\psi_S$  and axial ratio. Finally, we study the strength of the 2175-Å dust bump which we find to depend on inclination and the presence of a bulge. All these empirical results relate to the spatial distribution of dust in galaxies, relative to stars of different ages.

In Section 2, we present our methodology, along with a brief summary of the formalism used to describe dust attenuation in galaxies. In Section 3, we describe the data sets used and provide details of the photometric information extracted from each one of them. In Section 4, we present the attenuation curves, the shape of which we characterize by measuring the slope in small wavelength ranges in Section 5. In this section, we also present the radial gradients, a comparison of attenuation in the emission lines and stellar continua, and the strength of the 2175-Å dust bump. In Section 6, we provide an empirically derived fitting formula to correct the SEDs of a wide range of star-forming galaxies for dust attenuation. Finally, in Section 7, we present a qualitative model for the local and global geometry of dust in galaxies, which is consistent with the majority of our results.

Throughout this paper, we compare our results to the MW, LMC and SMC extinction curves, and the local starburst attenuation curve of C00. We adopt the MW extinction curve of Cardelli, Clayton & Mathis (1989), which is defined over the wavelength range  $0.125 < \lambda/\mu\text{m} < 3.5$ , with the correction given by O’Donnell (1994) in the optical region  $0.3 < \lambda/\mu\text{m} < 0.9$ . We adopt the tabulated LMC

<sup>1</sup> We follow the standard terminology (e.g. Calzetti 2001): extinction = absorption + scattering out of the line of sight; attenuation = absorption + scattering into and out of the line of sight caused by local and global geometric effects.

and SMC-bar curves of Gordon et al. (2003), spline-interpolating on to our wavelength points.

Absolute quantities such as stellar mass and SFR are required to match pairs of galaxies, and for these, we assume the standard  $\Lambda$  cold dark matter cosmology with  $\Omega_M = 0.3$ ,  $\Omega_\Lambda = 0.7$  and  $h = 0.7$ . The attenuation curves are based on flux ratios and are therefore independent of cosmology, magnitude types and filter zero-points.

## 2 METHODOLOGY

The basic principle of our method is the same as that used to measure the dust extinction along lines of sight through the MW and Magellanic Clouds, where the SEDs of pairs of stars of similar spectral type are compared. Here, we calculate the ratio of pairs of galaxy SEDs, where one galaxy is more dusty than the other, combining many pairs to obtain a high-S/N measurement of the attenuation curve. Just as with sightlines to stars in the MW or local galaxies, the method is only valid where no significant bias exists between the spectral types of the more dusty and less dusty galaxies. To ensure this, we match galaxy pairs in gas-phase metallicity, specific SFR ( $\psi_S$ , corrected for dust attenuation using the ratio of  $H\alpha$  to  $H\beta$  luminosity), axial ratio and redshift.

To ensure that we always divide the SED of the dustier member of the pair with that of the less dusty member, we use the ratio of  $H\alpha$  to  $H\beta$  luminosity as a measure of *relative* dust content. Our method is independent of, and insensitive to, the *absolute* dust content of the galaxies. In Sections 4 and 5, we calculate the average attenuation curve for samples split by specific SFR ( $\psi_S$ ), axial ratio ( $b/a$ ) and stellar surface mass density ( $\mu^*$ ), in circular apertures of increasing physical size. We use the resulting attenuation curves to study the changing shape and amplitude of the attenuation curve with each of these properties. In Section 6, we provide an empirically derived prescription for the attenuation of starlight by dust in external galaxies as a function of their  $\psi_S$ ,  $b/a$  and  $\mu^*$ .

### 2.1 Background to dust attenuation laws

The many different formalisms used to describe dust curves necessitate a brief overview of the subject to allow orientation of our work relative to other papers in the literature.

Light emitted by stars in external galaxies is affected by dust in three different ways: (i) absorption; (ii) scattering out of the line of sight to the observer; and (iii) scattering into the line of sight to the observer. The first two combined is usually termed ‘extinction’. In this paper, we use the term ‘attenuation’ to mean the average loss of light after integration over all lines of sight to light sources throughout the entire galaxy, encompassing all effects arising from the local and global geometric configuration of the dust and stars.<sup>2</sup> We use the term ‘effective optical depth’ to describe the final observed optical depth, which is related to the attenuation through  $A_\lambda = 1.086\tau_\lambda$ . Because blue light is scattered and absorbed more than red light by dust grains, an overall ‘reddening’ of the light is observed. In this section, we introduce the basic formalism used to describe the effects of dust on the integrated light from galaxies. Calzetti (2001) gives an extensive review of the literature up until a decade ago, although note that the terminology differs in places from that adopted here.

<sup>2</sup> Some other papers refer to ‘single-line-of-sight’ attenuation, which includes effects (i)–(iii) but excludes global geometric effects.

The attenuation  $A_\lambda$ , in mag, at a given wavelength  $\lambda$  is given by

$$A_\lambda = -2.5 \log_{10} \left( \frac{I_\lambda^o}{I_\lambda^e} \right), \quad (1)$$

$$= -2.5 \log_{10} [\exp(-\tau_\lambda)], \quad (2)$$

$$= 1.086\tau_\lambda, \quad (3)$$

where  $I_\lambda^o$  is the observed luminosity,  $I_\lambda^e$  is the intrinsic (emitted) luminosity of the source and  $\tau_\lambda$  is the effective optical depth of the dust. Ultimately, it is this quantity that we wish to know in order to correct the SEDs of galaxies for dust attenuation.

Observationally, the measurement of the overall amplitude of extinction and reddening of light are usually separate tasks. It is therefore practical to separate the attenuation into two components, the amplitude (usually specified in the  $V$  band,  $\tau_V$ ) and the shape of the attenuation curve ( $Q_\lambda$ )<sup>3</sup>:

$$\tau_\lambda = \tau_V Q_\lambda, \quad (4)$$

where  $Q_V = 1$ . In the case of extinction,  $Q_\lambda$  is a function of the distribution of grain composition, size and shape. When studying the integrated light from external galaxies,  $Q_\lambda$  is additionally a function of the *local geometry* of the dust and stars, and the *global geometry* of the galaxy (bulge and disc, and inclination).

Extinction curves have been measured along sightlines towards stars in the MW, LMC and SMC. While the average curves of the three galaxies are apparently entirely distinct, the individual sightlines in all three galaxies show a continuum of properties from steep slopes with weak 2175-Å dust bumps like the average SMC-bar curve to shallow slopes with strong bumps like the MW curve (Gordon et al. 2003). Unfortunately, current data are not good enough to determine robustly the ‘hidden parameter(s)’ responsible for this variation, although grain destruction by local star formation is often assumed.

The attenuation suffered by light from stars in nearby starburst galaxies, where the unattenuated stellar continuum varies relatively little between galaxies, has been measured empirically from the UV to NIR in a series of papers by D. Calzetti and collaborators (Calzetti et al. 1994; Kinney et al. 1994; Calzetti 1997a; Böker et al. 1999; C00). The attenuation curve was found to be ‘greyer’ (i.e. flatter) in the optical than the MW extinction curve, qualitatively as expected from the geometrical effects of mixed dust and stars. Additionally, no evidence was found for a strong ‘2175-Å’ dust feature which is observed in the majority of extinction curves measured along lines of sight in the MW (but see Noll et al. 2009; Conroy et al. 2010, and Section 5.5).

### 2.2 Measuring dust attenuation curves from pair-matched galaxy samples

An observed galaxy SED can be described as an intrinsic SED of unit stellar mass ( $I_\lambda^e$ ), multiplied by factors to account for the total stellar mass, cosmological distance of the galaxy and internal dust attenuation. Ideally, the two factors of normalization should be estimated from a region of the SED that is not attenuated by dust. In this paper, the longest wavelength point available to us is the  $K$  band at 2.2  $\mu\text{m}$ . We therefore normalize each galaxy by its  $K$ -band flux and retain a small correction factor throughout this work

<sup>3</sup> Conversions between different parametrizations of attenuation curve shapes are  $\frac{A_\lambda}{E(B-V)} \frac{E(B-V)}{A_V} = \frac{k_\lambda}{k_V} = \frac{\tau_\lambda}{\tau_V} = Q_\lambda$ .

which allows for small amount of dust attenuation in the  $K$  band ( $\Delta\tau_K$ ) during the fitting procedures. The normalized SED ( $F_\lambda$ ) can be written as

$$F_\lambda = \frac{I_\lambda^e N}{f_K} \exp(-\tau_\lambda), \quad (5)$$

where  $N$  accounts for the stellar mass and cosmological distance,  $\exp(-\tau_\lambda)$  for the internal dust attenuation and  $f_K$  is the observed  $K$ -band flux.

Directly from equation (5), the ratio of a pair of normalized galaxy SEDs (labelled 1 and 2), where both members of the pair have the same intrinsic SED but different dust contents and absolute normalizations, can be written after some algebra as

$$\left(\frac{F_1}{F_2}\right)_\lambda = \exp(-\Delta\tau_\lambda + \Delta\tau_K), \quad (6)$$

where  $\Delta\tau_\lambda \equiv \tau_{\lambda,1} - \tau_{\lambda,2}$  and  $\Delta\tau_K$  accounts for the small, unknown extinction in the  $K$  band. The geometric mean<sup>4</sup> of a sample of flux ratios, where in each pair galaxy  $F_1$  is more dusty than galaxy  $F_2$ , results in a dust attenuation curve normalized to zero at the  $K$  band which we denote by  $\overline{\mathcal{T}}_\lambda$  to distinguish it from the true attenuation:

$$\overline{\mathcal{T}}_\lambda = \frac{1}{n} \sum_{i=1}^n \ln \left( \frac{F_{1,i}}{F_{2,i}} \right)_\lambda \quad (7)$$

$$= -\langle \Delta\tau_V \rangle Q_\lambda + \langle \Delta\tau_K \rangle, \quad (8)$$

where  $n$  is the number of pairs of galaxies in the sum,  $\langle \Delta\tau_\lambda \rangle$  is the arithmetic mean of the difference in dust attenuation between galaxies 1 and 2, and we have expanded  $\Delta\tau_\lambda$  into the *amplitude* of attenuation at 5500 Å ( $\Delta\tau_V$ ) and the *shape* of the attenuation curve ( $Q_\lambda$ ), as described above. From now on we will drop the brackets and write simply  $\Delta\tau$  as the effective optical depth averaged over multiple galaxy pairs.

Some points to note about the method are as follows:

(i) Because we are working with broad-band photometry, strictly equation (5) should include an integration over the filter response function ( $R_\lambda$ ). In the case where  $Q_\lambda$  varies with  $\lambda$  over the wavelength range of the filter, it can be shown that we measure  $\int Q_\lambda R_\lambda d\lambda$  rather than  $Q_\lambda$ , even in the case where  $I_\lambda^e$  varies with  $\lambda$ . Due to the generally weak variation of attenuation curves with  $\lambda$ , this distinction is only important in the UV (Section 5.5) and we have therefore omitted the integrand for clarity.

(ii) Equation (8) holds only in the case where  $Q_\lambda$  is the same for both members of the pair, that is, when there is no trend between  $Q_\lambda$  and dust content. See Appendix A and Fig. A1 for the result of tests showing that this is the case in our samples.

(iii)  $Q_\lambda$  may be different for different pairs in the sum; in this case, the measured  $Q_\lambda$  will be the  $\Delta\tau_V$  weighted mean  $Q_\lambda$  of the sample.

(iv) The method does not require that the intrinsic stellar populations are exactly the same in each galaxy pair; any residual stellar population remaining after the division of the two SEDs will only add noise to the final measurement. However, it does require that there is no systematic correlation between the residual and the dust content of the galaxy. See Appendix A and Fig. A2 for an example of how such a correlation can occur using photometry to estimate  $\psi_S$  rather than the  $H\alpha$  emission line.

<sup>4</sup> The geometric mean of flux ratios is preferred for dust curves, as this is equivalent to the arithmetic mean of the log of flux ratios, which is directly related to optical depth.

(v) The method is almost, but not quite, the same as that employed by Calzetti et al. (1994, 2000, 2007) for starburst galaxies:

(a) They use a single ‘dust-free’ composite spectrum with which to compare dustier composite spectra. Because we use a whole range of types of galaxies, with many different shapes of SEDs, we first define strict galaxy pairs, the SEDs of which we divide before combining galaxies into samples. This approach makes our method more robust, as each pair is treated individually meaning outliers can be easily identified and removed. Additionally, errors can be estimated on the resulting attenuation curves.

(b) Each of our binned samples of galaxies contains 14–40 times more galaxies than the original starburst sample of Calzetti et al. (1994) which contained 39 galaxies.

(c) We define the attenuation curve in terms of the shape of the curve ( $Q_\lambda$ ) and the amplitude of attenuation in the *stellar continuum* at the  $V$  band ( $\tau_V$ ). This differs in formalism from that of Calzetti et al. (2000) who directly incorporate the amplitude of dust attenuation in the emission lines into the attenuation curve for the stellar continuum.

### 2.3 Pair-matching procedure

In order to achieve the requirement for a close match in intrinsic stellar population, we identify pairs of galaxies that match in metallicity,  $\psi_S$ ,  $b/a$  and redshift. The restrictions on metallicity and  $\psi_S$  are to ensure that both galaxies have similar intrinsic SEDs. The restriction on  $b/a$  also minimizes the effect of seeing different stellar populations in inclined versus face-on galaxies simply due to changes in transparency.

In order to identify galaxies which are more or less dusty, we use the ratio of  $H\alpha$  to  $H\beta$  luminosity measured from the SDSS spectra. At this stage, the sole purpose of using this line ratio as a measure of dust content is to ensure that, in as many pairs as possible, the denominator SED is more dusty than the numerator in equation (7). Only in this case will we measure an overall attenuation.

Because the  $H\alpha$  and  $H\beta$  emission lines are measured within a small fixed angular aperture (see Section 3.1), and radial gradients in dust exist, both galaxies in the pair must have the same redshift to minimize the numbers of pairs in which the denominator SED is in fact less dusty than the numerator simply because the lines are measured from different regions of each member of the pair. The restriction on redshift also means that galaxy pairs do not need to be corrected for any relative shifting of bandpasses with redshift, as the photometric bands probe the same rest-frame wavelength of the SED in each member of the pair.

The procedure is as follows. The galaxies are ordered by increasing ratio of  $H\alpha$  to  $H\beta$  luminosity, and starting from the least dusty galaxy in the sample, the dustiest suitable partner is found using the criteria mentioned above. We require that there is a significant difference between the dust contents of galaxy pairs, as measured by the difference in emission-line optical depth. This maximizes the S/N of the final attenuation curves, by excluding pairs which contribute only noise and no signal.

To summarize the pair-matching criteria:

- (i)  $|\Delta \log O/H| < 0.05$ ,
- (ii)  $|\Delta \log \psi_S| < 0.1$ ,
- (iii)  $|\Delta(b/a)| < 0.1$ ,
- (iv)  $|\Delta z| < 0.01$ ,
- (v)  $\Delta\tau_{V,\text{line}} > 0.2$ .

Details of how the derived quantities are measured are given in Section 3. If a suitable pair is not found, the initial galaxy is

removed from the sample, and the algorithm moves on to the next galaxy. Once a pair has been identified, both members are removed from the sample; thus, each galaxy can contribute only once to the attenuation curve.

Once all possible pairs have been identified within a particular sample, the galaxy SEDs are normalized by their  $K$ -band flux and the flux ratios calculated in each band for each pair. These flux ratios are combined using a geometric mean (equation 7). A preliminary stack is made, outlying pairs with flux ratios which are in the upper or lower 1 per cent of the distribution in any band are removed from the sample, and the attenuation curves recalculated using the cleaned sample.

We verified that the precise details of the pair-matching criteria given above are unimportant to the final results by varying the widths of the bins and repeating our analysis. Tests showed that the best S/N was achieved when the difference between the dustiness of each pair of galaxies is maximized. We verified that selecting pairs to have approximately the same  $\Delta\tau_{V,\text{line}}$  instead does not significantly alter the results (see Fig. A1). Additionally, we repeated our analysis replacing the pair-match on metallicity with a pair-match on stellar mass or stellar surface mass density. These latter quantities are global measurements from the total SDSS photometry, whereas metallicity is measured from the central 3 arcsec of the galaxies. Once again, our results were generally found to be not sensitive to exactly which properties we used in the pair-matching, presumably by virtue of the observed strong relations between these parameters. Where differences were found, they were consistent with our expectation that dustier galaxies have higher metallicities and therefore redder intrinsic SEDs, therefore a failure to match on metallicity results in a slight bias in the attenuation curves as discussed in the previous subsection.

We note that no correction is applied for the shifting of the photometric bands with redshift ( $K$ -correction). We attempted to correct each SED ratio for this shifting, using an iterative approach in which

the previously derived attenuation curve was used to determine the small corrections to apply to each flux ratio. However, this was found to make no difference to the results. The smoothness of the attenuation curves compared to individual galaxy SEDs, the similar redshift of both members of the pairs, and the relatively small redshift range covered by the majority of the galaxies (70 per cent with  $0.03 < z < 0.09$ ) likely all help to minimize the effects. For the final derivation of the attenuation curve in Section 6, the  $K$ -correction is irrelevant as all pairs are combined at their correct rest-frame wavelength.

### 3 THE DATA SETS

In order to measure the dust attenuation curves from the UV to the NIR, in a wide range of star-forming galaxies, we combine three of the largest modern-day astronomical data sets: the SDSS in the optical; the UKIRT Infrared Deep Sky Survey (UKIDSS) in the NIR; and the *Galaxy Evolution Explorer* (*GALEX*) in the UV.

All fluxes are corrected for Galactic extinction using the values provided in the respective catalogues which are based upon the Schlegel, Finkbeiner & Davis (1998) dust emission maps and the MW extinction curve of Cardelli et al. (1989), with a small correction in the optical wavelength regime of O'Donnell (1994). The *GALEX* catalogue provides  $E(B - V)$  which we convert into extinction for the UV fluxes using the MW extinction curve.

Fig. 1 shows the distributions of redshift and physical properties for the galaxies used in this paper.

#### 3.1 The SDSS spectroscopic survey

The SDSS is an optical photometric and spectroscopic survey of local galaxies. The final data release (DR7, Abazajian et al. 2009) includes 9380 deg<sup>2</sup> with spectroscopic coverage, targeting nearly 10<sup>6</sup> galaxies with Petrosian  $r$ -band magnitudes  $< 17.77$ . The

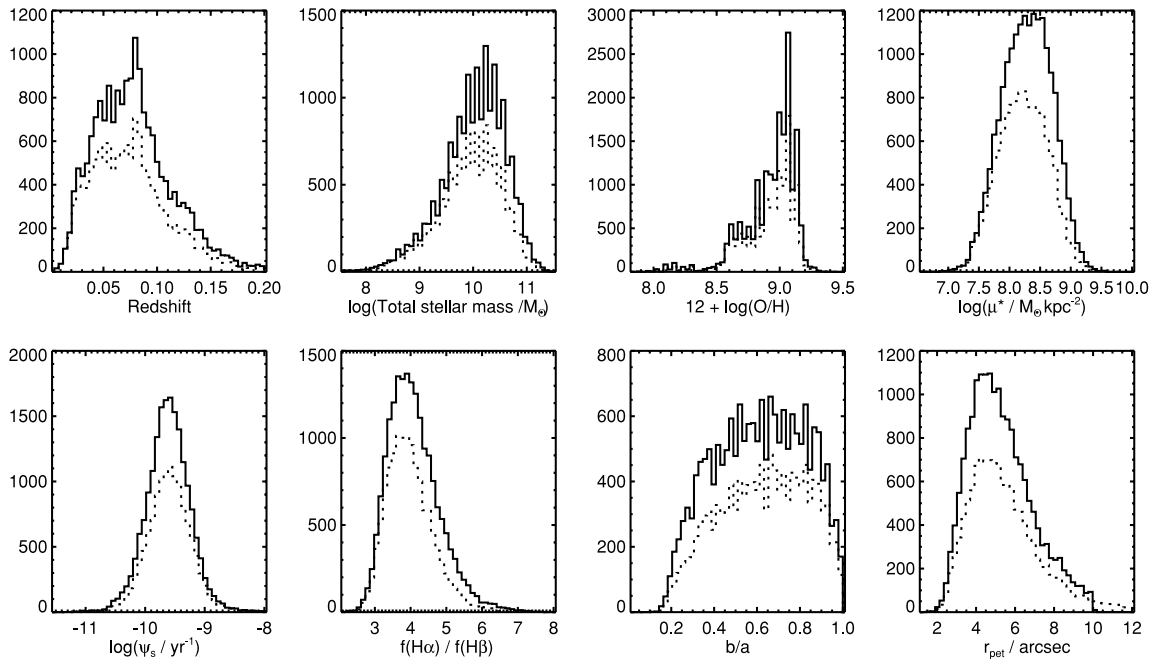


**Figure 1.** Distribution of basic galaxy properties for the full sample (solid line) and UV sample (dotted line). Individual panels show (a) redshift; (b) total stellar mass measured from SED fitting to the five-band SDSS photometry; (c) gas-phase metallicity in the central 3 arcsec; (d) stellar surface mass density, calculated from the physical size measured in the  $z$  band and total stellar mass; (e) specific SFR ( $\psi_s$ ) measured within the central 3 arcsec; (f) ratio of  $H\alpha$  to  $H\beta$  luminosity; (g) axial ratio, measured in the  $r$  band; and (h)  $r$ -band Petrosian radius in arcsec.

spectra have good S/N and moderate resolution which allows for the deconvolution of stellar continuum from nebular emission that is crucial to accurately measure the H $\alpha$  and H $\beta$  line strengths. Such a deconvolution has been carried out by Brinchmann et al. (2004) and Tremonti et al. (2004), and the emission-line measurements are available online.<sup>5</sup> The SDSS provides the  $u$ ,  $g$ ,  $r$ ,  $i$ ,  $z$  aperture photometry used in this paper, with the central effective wavelengths ( $\lambda_{\text{eff}}$ ) of 3546, 4670, 6156, 7471 and 8918 Å, respectively (Schneider, Gunn & Hoessel 1983; Fukugita et al. 1996). The SQL query used to extract the parameters from the SDSS Catalog Archive Server is provided in Appendix B. A total of 797 026 unique galaxies are extracted from the catalogue, with 552 577 that have spectral per-pixel S/N > 6 in the  $g$  band are in the SDSS-MPA data base and have ‘best’ magnitudes within the formal survey requirements ( $14.5 < m_r < 17.77$ ), where  $m_r$  is the  $r$ -band Petrosian magnitude corrected for Galactic extinction.

Because we are interested in the interstellar medium (ISM) properties of star-forming galaxies, we use the [N II]/H $\alpha$  and [O III]/H $\beta$  emission-line ratios (Baldwin, Phillips & Terlevich 1981, BPT ratios) to remove galaxies which show signs of an active galactic nucleus, selecting only those galaxies that lie below the demarcation line of Kauffmann et al. (2003b). We also select only those galaxies with all four lines measured at  $>3\sigma$  confidence, after scaling the formal errors by the scaling factors suggested in the SDSS-MPA web pages. This results in 140 737 galaxies.

The parameters that we extract from the SDSS catalogues are as follows:

(i) *Emission-line dust* ( $\tau_{V,\text{line}}$ ). The H $\alpha$  and H $\beta$  line fluxes, measured after accurate subtraction of the underlying stellar continuum, give the total dust attenuation suffered by the emission lines at 5500 Å. We assume the dust attenuation curve for emission lines of Wild et al. (2011):  $\tau_{V,\text{line}} = 3.226 \ln(f_{\text{H}\alpha}/f_{\text{H}\beta})_{\text{obs}} - 3.226 \ln(f_{\text{H}\alpha}/f_{\text{H}\beta})_{\text{int}}$ . This was measured through a comparison of the luminosity of mid-IR and optical emission lines. In the case that the dust-free intrinsic line ratio  $[(f_{\text{H}\alpha}/f_{\text{H}\beta})_{\text{int}}]$  is the same for both galaxies in a pair, this term cancels when the ratio of two galaxy SEDs is calculated.<sup>6</sup>

(ii) *Stellar mass* ( $M^*$ ). Measured from the five-band SDSS Petrosian photometry in units of solar mass using a Bayesian fit to a library of stochastic star formation histories similar to those used in Gallazzi et al. (2005) and are publicly available.<sup>7</sup> Stellar masses are calculated from both total and fibre photometry.

(iii) *Star formation rate*. Calculated from the dust-corrected H $\alpha$  luminosities, using the conversion factor of Kennicutt (1998) and  $\tau_{V,\text{line}}$  given above. We do not use the SFR of Brinchmann et al. (2004) as this assumes a different dust attenuation curve. The precise conversions assumed to calculate SFR from H $\alpha$  luminosity do not affect our final results. Specific SFR ( $\psi_S$ ) is calculated as  $\text{SFR}/M_{\text{fib}}^*$ . It was found that  $\psi_S$  calculated from the five-band SDSS

photometry alone was not a good enough estimate of the intrinsic spectral shape of the galaxies (see Appendix A and Fig. A2).

(iv) *Gas-phase metallicity*. Measured from a combination of the strongest optical emission-line fluxes by Tremonti et al. (2004), using the method of Charlot & Longhetti (2001).

(v) *Stellar surface mass density* ( $\mu^*$ ). Calculated as  $M^*/(2\pi r^2)$ , where  $r$  is the physical size in kpc of the radius which contains 50 per cent of the  $z$ -band Petrosian flux. The  $z$  band probes the older stellar population and thus gives greater weight to galaxy bulges than a bluer band would do.

(vi) *Size*. We adopt the  $r$ -band Petrosian radius as a measure of the size of the galaxies. This is the radius at which the ratio of local surface brightness to mean surface brightness is 0.2. The  $r$  band probes both young and old populations with almost equal weight in star-forming galaxies and therefore provides a good average measure of galaxy size.

(vii) *Inclination* ( $b/a$ ). The exponential profile axial ratio measured in the  $r$  band which has the highest S/N of all red SDSS bands. The majority of our star-forming sample are expected to be disc galaxies, and therefore the exponential profile fit is the most appropriate. A detailed study of the link between  $b/a$  and the physical shape of galaxies in the SDSS is given by Maller et al. (2009).

(viii) *Recent star formation history*. We remove all galaxies with post-starburst spectral features using the method of Wild et al. (2007). These galaxies have unusual SED shapes which may correlate with dust, thus causing problems during our pair-matching procedure.

A feature of the SDSS is that the spectra are observed through 3-arcsec-diameter optical fibres, therefore probing a small central fraction of the total light of the galaxies. For the main focus of this work, this ‘aperture bias’ is irrelevant as we use the spectroscopic information primarily to identify relative dust content. Where necessary, that is, when we compare fibre and photometric quantities, we use photometry extracted in  $\sim 3$  arcsec apertures.

### 3.2 The UKIDSS Large Area Survey

We match the SDSS catalogue resulting from the previous subsection with the seventh data release of the ongoing UKIDSS Large Area Survey (LAS, Lawrence et al. 2007) to obtain NIR  $Y$ ,  $J$ ,  $H$ ,  $K$  photometry for the galaxies ( $\lambda_{\text{eff}} = 1.0305, 1.2483, 1.6313, 2.2010 \mu\text{m}$ ). The UKIDSS uses the UKIRT Wide Field Camera (WFCAM, Casali et al. 2007), the photometric system is described in Hewett et al. (2006), the calibration in Hodgkin et al. (2009) and the science archive in Hambly et al. (2008). We locate all objects with SDSS–UKIDSS cross-matches within 2 arcsec and select the nearest neighbour if more than one match exists. We exclude all galaxies for which photometry has been ‘de-blended’. Problems with the UKIDSS pipeline mean that the flux in such objects is overestimated (Hill et al. 2010). The SQL query used to extract the parameters from the UKIDSS online data base, and cross-match the SDSS and UKIDSS catalogues, is provided in Appendix B. The UKIDSS–SDSS cross-match results in our primary optical–NIR sample of 22 902 star-forming galaxies.

### 3.3 The GALEX All-Sky Imaging Survey

There is considerable interest in the shape of the attenuation curve in the rest-frame UV wavelength range, particularly for high-redshift galaxy studies. Therefore, we build a second, smaller galaxy sample in which we match our optical–NIR galaxy sample to the GALEX All-Sky Imaging Survey (AIS, Martin et al. 2005) catalogue. The

<sup>5</sup> <http://www.mpa-garching.mpg.de/SDSS>

<sup>6</sup> The intrinsic line ratio depends upon  $T_e$ ,  $n_e$  and  $Z$  and therefore varies slightly with galaxy type and dust content. Over most of parameter space relevant to galaxies, this causes a variation in true optical depth for a given observed line ratio at a level of less than 10 per cent. However, for massive, high-metallicity galaxies with low dust contents, optical depths can be up to a factor of 2 lower than predicted from the observed line ratio, assuming a standard intrinsic ratio of 2.87. This effect cannot bias our attenuation curves, but may act as an additional source of noise in certain bins.

<sup>7</sup> <http://www.mpa-garching.mpg.de/SDSS/DR7/Data/stellarmass.html>

SQL query used to query the *GALEX*-MAST data base<sup>8</sup> is shown in Appendix B. We use the table xSDSSDR7 to identify the closest (rank 1) galaxies within 2 arcsec (Budavári et al. 2009)<sup>9</sup> and retain only those galaxies with both near-UV ( $\lambda_{\text{eff}} = 2267 \text{ \AA}$ ) and far-UV ( $\lambda_{\text{eff}} = 1516 \text{ \AA}$ ) fluxes measured at greater than  $3\sigma$  confidence. This second UKIDSS–SDSS–*GALEX* sample contains 15 305 galaxies.

### 3.4 Aperture photometry

The precision to which extremely large modern surveys allow us to measure stacked quantities demands the use of extreme care in the handling of the data if tiny systematics are not to dominate the final result. While our pair-matching methodology eliminates absolute offsets in photometric scales between different bands and data sets, relative offsets can cause notable errors. For example, radial gradients in the stellar populations and dust contents of galaxies mean that the use of different photometric apertures at different wavebands would result in incorrect results. Fortunately, both the SDSS and UKIDSS catalogues provide sets of aperture photometry measured with various circular aperture sizes. For each galaxy, we interpolate these annular flux densities on to a grid fixed relative to the galaxy’s *r*-band Petrosian radius ( $R_{\text{pet}}$ ). This allows us to calculate dust attenuation curves at fixed cumulative fractions of  $R_{\text{pet}}$ , namely 25, 35, 50, 70, 90 and 100 per cent. The large point spread function (PSF) of the *GALEX* ( $\sim 5$  arcsec full width at half-maximum) prevents a similar analysis of the UV data, for which we are restricted to a single ‘total’ magnitude.

Annular aperture photometry is provided in the SDSS catalogue at the radii of 0.23, 0.68, 1.03, 1.76, 3, 4.63, 7.43 and 11.42 arcsec, which we convert into cumulative fluxes. Similarly, cumulative aperture photometry is provided in the UKIDSS catalogue at the radii of 0.5, 0.71, 1, 1.41, 2, 2.83, 4, 5, 6, 7, 8 and 10 arcsec. For each galaxy, we linearly interpolate both sets of cumulative fluxes on to the grid of fixed fractions of  $R_{\text{pet}}$  given above. Although linear interpolation between measured apertures is not sufficiently accurate to obtain absolute magnitudes, it is entirely sufficient for our purpose of obtaining accurate dust curves.

The use of fixed-aperture photometry does not account for a changing PSF as a function of band or survey. However, the atmospheric seeing conditions under which the SDSS and UKIDSS photometries were obtained were generally excellent, and the PSF is typically smaller than  $0.35R_{\text{pet}}$  (the smallest aperture size that we analyse in Section 5) which is  $\gtrsim 1.5$  arcsec for galaxies in our sample. A small number of very extended galaxies with their Petrosian radius larger than the maximum apertures extracted from the catalogues were removed from the sample (see Section 3.1 for a definition of the Petrosian radius).

## 4 THE ATTENUATION CURVES

To begin with, we focus on measurements of the optical–NIR attenuation curves, for which the data are of a uniform and excellent quality, and the data sample larger. In Section 5.5, we study the reduced UV–NIR sample of galaxies.

We split the galaxies into two independent samples with low and high stellar surface mass density ( $\mu^*$ ), at the position of the bimodality observed in the local galaxy population  $\mu^* = 3 \times 10^8 \text{ M}_{\odot} \text{ kpc}^{-2}$  (Kauffmann et al. 2003a). We then define several subsamples in bins

of  $\log_{10}\psi_S$  and  $b/a$ . Table 1 presents the details of the samples. The measured attenuation curves are given in full for each sample and aperture in Table 2 (full table is available as Supporting Information with the online version of this paper).

The cut in  $\mu^*$  effectively separates bulge-less galaxies from galaxies with (even small) bulges. Comparing our  $\mu^*$  cut with results from the bulge-to-disc decomposition of Gadotti (2009), we find that while some pseudo-bulges have  $1 \times 10^8 < \mu^* < 3 \times 10^8$  and therefore fall into our bulge-less sample, classical bulges and ellipticals all have  $\mu^* > 3 \times 10^8$ . Radial gradients may be expected to be more prevalent in bulge+disc systems, and the presence of a bulge may significantly affect the attenuation of light from galaxies, compared to pure disc systems (Pierini et al. 2004). We therefore choose to treat these two samples independently.

Figs 2 and 3 show the attenuation curves for each bin. Different colour curves indicate different aperture sizes. To facilitate comparison between panels, the black line shows the dust curve derived from the whole sample and is the same in all panels. Some qualitative comparison between the different attenuation curves is instructive. First, we note that in most panels the overall normalization of the curves drops with decreasing aperture size, which is due to radial gradients in dust content. The inner radii are dustier and therefore a larger  $\Delta\tau$  is measured. We see that radial gradients are more notable in galaxies with higher  $\psi_S$ . We will present a quantitative study of the radial gradients in Section 5.3.

Secondly, the overall normalization of the curves in each panel depends on the range in dust content of the galaxies in the input sample, simply because of the method used to build the curves. A larger overall  $\Delta\tau_{V,\text{cont}}$  means a greater range of dust contents in the input sample. Both samples show a steady decrease in  $\Delta\tau_{V,\text{cont}}$  with increasing  $b/a$  and increase in  $\Delta\tau_{V,\text{cont}}$  with increasing  $\psi_S$ . This implies that high  $\psi_S$  and more inclined galaxies exhibit a larger range of  $\Delta\tau_{V,\text{cont}}$ . This pure selection effect does not affect our results, which depend only on the shape of the attenuation curve, or its amplitude relative to another dust indicator.

It is notable from Table 1 that the bins of  $\psi_S$  and axial ratio are not entirely independent: when binning by  $\psi_S$ , bins with lower  $\psi_S$  have lower median axial ratios; similarly when binning by axial ratio, bins with lower  $b/a$  have higher median  $\psi_S$ . Indeed, when investigating the whole data set, there is a small but significant positive trend between  $\psi_S$  and axial ratio, which cannot be a ‘fundamental’ property of galaxies, but, as we shall show later in this paper, it is likely an effect of dust. A bias in an observational property such as this one can cause an intrinsic property to correlate with dust content and ultimately bias the shape of the attenuation curve. In this case, it shows the importance of pair-matching galaxies in  $b/a$ .

In the following section, we begin our quantitative study of the attenuation curves of the binned samples by parametrizing them using a simple analytic form, which allows for easy visualization of changes in shape and amplitude with galaxy properties.

## 5 TRENDS OF ATTENUATION WITH GALAXY PROPERTIES

As discussed in Section 1, the shape of the dust attenuation curve, and the strength relative to the ratio of  $H\alpha$  to  $H\beta$  luminosity, can tell us about the dust properties and dust–star geometry within galaxies. In order to visualize trends in the attenuation curves presented in Figs 2 and 3, we must first parametrize the curves. After some experimentation, a broken power law was found to provide an adequate representation of the optical–NIR data, with easily interpretable fitted parameters. A single power law was unable to fit

<sup>8</sup> <http://galex.stsci.edu/casjobs/>

<sup>9</sup> <http://galex.stsci.edu/doc/CASJobsXTutorial.htm>

**Table 1.** Number of pairs, median redshift, median  $\psi_S$ , median  $b/a$  and mean  $\Delta\tau_{V,\text{line}}$  for each SDSS+UKIDSS sample.

	$n_{\text{pair}}$	$\bar{z}$	$\overline{\log(\psi_S)}$	$\overline{(b/a)}$	$\Delta\tau_{V,\text{line}}$
$\mu^* < 3 \times 10^8$					
All galaxies	3431	0.067	-9.62	0.62	$0.60^{+0.00}_{-0.00}$
-11.00 < $\log(\psi_S/\text{yr}^{-1})$ < -9.90	541	0.060	-10.03	0.55	$0.65^{+0.02}_{-0.01}$
-9.90 < $\log(\psi_S/\text{yr}^{-1})$ < -9.75	547	0.069	-9.82	0.61	$0.62^{+0.01}_{-0.01}$
-9.75 < $\log(\psi_S/\text{yr}^{-1})$ < -9.62	578	0.072	-9.68	0.66	$0.59^{+0.01}_{-0.01}$
-9.62 < $\log(\psi_S/\text{yr}^{-1})$ < -9.46	689	0.072	-9.54	0.64	$0.60^{+0.01}_{-0.01}$
-9.46 < $\log(\psi_S/\text{yr}^{-1})$ < -9.25	613	0.069	-9.37	0.65	$0.56^{+0.01}_{-0.01}$
-9.25 < $\log(\psi_S/\text{yr}^{-1})$ < -7.90	366	0.057	-9.12	0.60	$0.53^{+0.02}_{-0.02}$
0.0 < $b/a$ < 0.4	896	0.056	-9.68	0.34	$0.69^{+0.01}_{-0.01}$
0.4 < $b/a$ < 0.6	911	0.065	-9.60	0.55	$0.60^{+0.01}_{-0.01}$
0.6 < $b/a$ < 0.8	697	0.074	-9.60	0.72	$0.55^{+0.01}_{-0.01}$
0.8 < $b/a$ < 1.0	721	0.077	-9.61	0.87	$0.55^{+0.01}_{-0.01}$
$\mu^* > 3 \times 10^8$					
All galaxies	1877	0.083	-9.75	0.62	$0.72^{+0.01}_{-0.01}$
-11.00 < $\log(\psi_S/\text{yr}^{-1})$ < -9.90	503	0.079	-10.09	0.58	$0.70^{+0.01}_{-0.02}$
-9.90 < $\log(\psi_S/\text{yr}^{-1})$ < -9.75	334	0.086	-9.82	0.59	$0.70^{+0.02}_{-0.02}$
-9.75 < $\log(\psi_S/\text{yr}^{-1})$ < -9.62	290	0.092	-9.69	0.62	$0.72^{+0.03}_{-0.02}$
-9.62 < $\log(\psi_S/\text{yr}^{-1})$ < -9.46	314	0.086	-9.55	0.65	$0.69^{+0.02}_{-0.02}$
-9.46 < $\log(\psi_S/\text{yr}^{-1})$ < -7.90	359	0.085	-9.32	0.72	$0.73^{+0.03}_{-0.02}$
0.0 < $b/a$ < 0.4	485	0.071	-9.88	0.35	$0.75^{+0.02}_{-0.02}$
0.4 < $b/a$ < 0.6	555	0.084	-9.72	0.55	$0.73^{+0.02}_{-0.02}$
0.6 < $b/a$ < 0.8	399	0.090	-9.69	0.72	$0.70^{+0.02}_{-0.02}$
0.8 < $b/a$ < 1.0	349	0.089	-9.70	0.88	$0.63^{+0.02}_{-0.02}$

**Table 2.** Averaged attenuation curves, normalized to zero at  $K$  ( $\mathcal{T}_\lambda$ , equation 7), for each sample studied in this paper (full table is available as Supporting Information with the online version of this paper).

Sample	Aperture	$u$	$g$	$r$	$i$	$z$	$Y$	$J$	$H$
All galaxies	$0.25R_{\text{pet}}$	-0.493	-0.362	-0.261	-0.209	-0.161	-0.123	-0.074	-0.042
	$0.35R_{\text{pet}}$	-0.473	-0.349	-0.250	-0.200	-0.153	-0.116	-0.068	-0.038
	$0.50R_{\text{pet}}$	-0.455	-0.336	-0.239	-0.192	-0.146	-0.110	-0.062	-0.035
	$0.70R_{\text{pet}}$	-0.439	-0.325	-0.231	-0.186	-0.141	-0.105	-0.056	-0.033
	$0.90R_{\text{pet}}$	-0.431	-0.319	-0.227	-0.183	-0.139	-0.101	-0.054	-0.032
	$1.00R_{\text{pet}}$	-0.428	-0.316	-0.225	-0.182	-0.138	-0.100	-0.054	-0.032
	3 arcsec	-0.484	-0.355	-0.253	-0.202	-0.154	-0.119	-0.069	-0.038

the whole wavelength range, due to a change in the slope between the optical and NIR wavelength regimes. We fit this function using a least-squares minimization routine, weighting each data point equally:

$$\begin{aligned} \mathcal{T}_\lambda &= -\Delta\tau_{\lambda_c} \left(\frac{\lambda}{\lambda_c}\right)^{s_{\text{opt}}} + \Delta\tau_K & \lambda < \lambda_c \\ &= -\Delta\tau_{\lambda_c} \left(\frac{\lambda}{\lambda_c}\right)^{s_{\text{nir}}} + \Delta\tau_K, & \lambda > \lambda_c \end{aligned} \quad (9)$$

where the free parameters describe the wavelength at which the shape of the attenuation curve changes between the optical and the NIR ( $\lambda_c$ ), the mean amplitude of the attenuation curve at this wavelength ( $\Delta\tau_{\lambda_c}$ ), the mean amplitude of the attenuation curve at the longest wavelength point ( $\Delta\tau_K$ ), and the power-law slope of the attenuation curve in the optical ( $s_{\text{opt}}$ ) and in the NIR ( $s_{\text{nir}}$ ). In this section, our aim is only to measure the slope of the curves for the purpose of visualization. Therefore, we fit only the  $u$ ,  $g$ ,

$r$ ,  $i$ ,  $Y$ ,  $J$ ,  $H$  and  $K$  bands, excluding the  $z$  band because of its proximity to the break in slopes at  $\lambda_c$ . For the same reason, we do not constrain the amplitudes of the two power laws ( $\Delta\tau_{\lambda_c}$ ) to be equal. In practice, the amplitudes of the two functions are similar. Note that by construction the form of this function is the same as that derived in equation (8), with  $Q_\lambda \propto \lambda^s$ .

Bootstrap errors on each of these parameters are estimated by recalculating the geometric mean, using random resampling with replacement of the galaxy pairs that contribute. We randomly select 100 samples of the same size as the original data set, and repeat the least-squares fitting on each sample. The 16th and 84th percentiles on each parameter are taken to be the  $1\sigma$  errors. We verified that increasing the number of samples to 500 does not change the resulting estimated errors.

Figs 2 and 3 show that even in samples exhibiting strong radial gradients, the attenuation curves are close to converged between 90

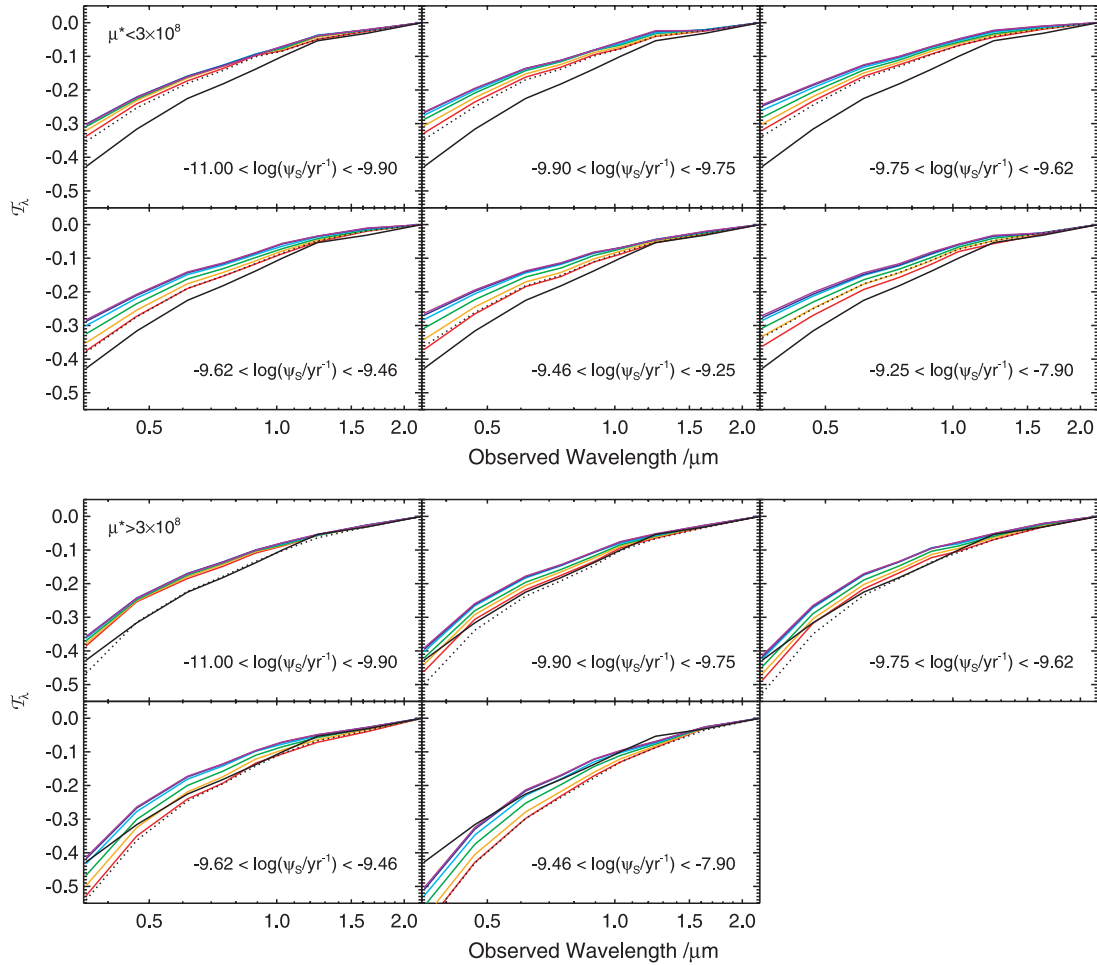


**Figure 2.** Averaged dust attenuation curves, normalized to zero at  $K$  (equation 7). Each panel shows galaxies in bins of  $\psi_S$ : with  $\log \mu^* < 8.3$  (top panels) and with  $\log \mu^* > 8.3$  (bottom panels). Note that the overall normalization of the curves in each panel depends on the range in dust content of the galaxies that make up each sample, and is thus somewhat arbitrary (see Section 4). Different colour lines indicate different physical aperture sizes, from red to purple: 25, 35, 50, 70, 90 and 100 per cent of the Petrosian  $r$ -band radius. In some panels, the curves show a progressively lower normalization with decreasing aperture size. This is caused by larger dust contents in the central regions of the galaxies. The dotted black line shows the attenuation curve when a 1.76-arcsec-radius angular aperture is used, close to the aperture through which the SDSS spectra are taken. To aid comparison between panels, the full black line is the attenuation curve measured at 90 per cent  $R_{\text{pet}}$  using all galaxies, and is the same in each panel.

and 100 per cent of  $R_{\text{pet}}$ . The fitted parameters at 90 and 100 per cent of  $R_{\text{pet}}$  are equal within the errors, but the errors at 90 per cent are smaller and trends tighter. This is possibly caused by increasing sky-subtraction errors at large radii in the UKIDSS photometry. Therefore, unless otherwise stated, we measure the galaxy-wide attenuation curves at 90 per cent of  $R_{\text{pet}}$ .

The fit is performed at the median rest frame of the galaxies in the sample (the median redshift is given in Table 1). As mentioned in Section 2.3, iteratively  $K$ -correcting the individual flux ratios before combining them into the dust attenuation curve makes no significant difference to the results and was therefore discarded from the final analysis.

The resulting fitted parameters and errors are given in Table 3, together with comparison numbers for curves in the literature measured in exactly the same way as our data. As expected, the fitted  $\Delta\tau_K$  values are close to zero, with their exact values imposed by the constraint that the NIR slope is a perfect power law. In the following subsections, we present the trends of attenuation curve shape, radial gradients, and difference between nebular-line and stellar contin-

uum attenuation as a function of  $\psi_S$  and axial ratio, for both high- and low- $\mu^*$  galaxies.

### 5.1 The slope of the attenuation curve in the optical

Fig. 4 presents the optical slopes of the attenuation curves ( $s_{\text{opt}}$ ) as a function of  $\psi_S$  and  $b/a$ . The dotted horizontal lines indicate the slopes of the MW, C00, LMC and SMC-bar curves measured using the same method. There are significant trends in optical slope with galaxy properties. In both high- and low- $\mu^*$  samples, the curve flattens slowly with decreasing axial ratio, meaning greayer curves in edge-on galaxies and steeper curves in face-on galaxies. This is the first clear example of global geometry affecting the apparent attenuation curves of galaxies.

The high- $\mu^*$  sample exhibit steeper optical slopes than the low- $\mu^*$  sample, and significantly steeper even than the MW extinction curve. This is intriguing as attenuation curves resulting from mixed stars and dust in galaxies are generally expected to be flatter than the underlying extinction curves. Steeper optical extinction curves

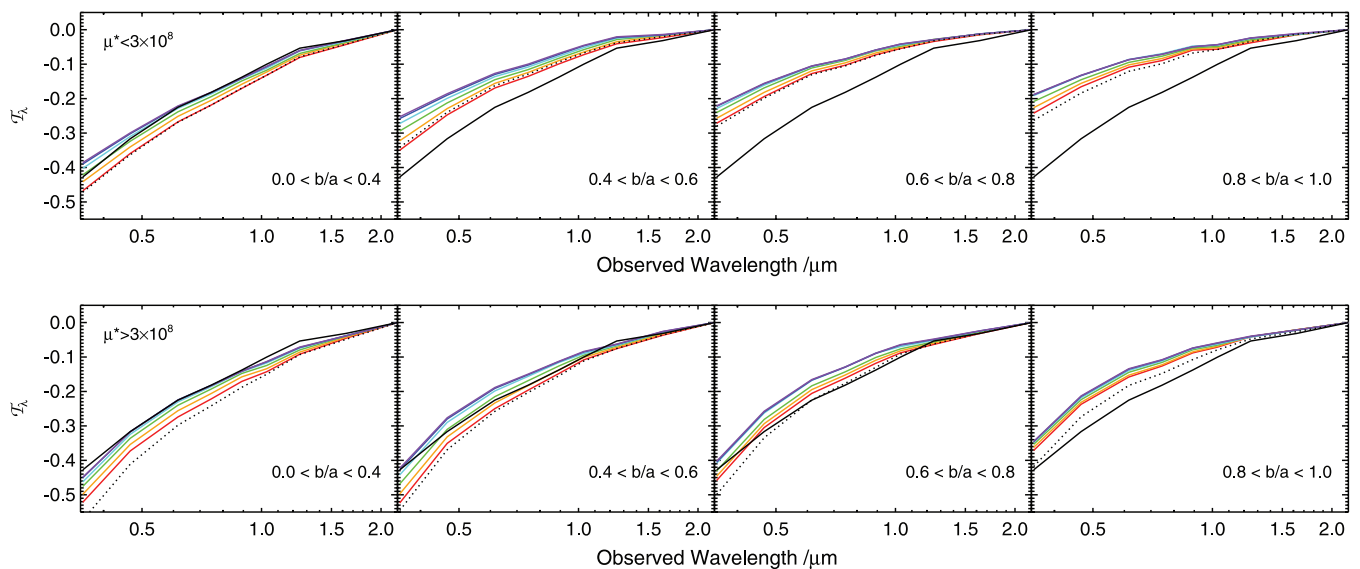


**Figure 3.** Averaged dust attenuation curves, normalized to zero at  $K$  (see equation 7). Each panel shows galaxies in bins of axial ratio ( $a/b$ ): with  $\log \mu^* < 8.3$  (top panels) and with  $\log \mu^* > 8.3$  (bottom panels). Lines are as in Fig. 2.

do exist locally in the SMC and actively star-forming regions in the MW, possibly caused by the modification of grain composition. However, it would be surprising if massive, metal-rich, bulge-dominated galaxies have grain compositions closer to active dwarf galaxies than to the MW. Steeper apparent slopes could be caused by a mismatch in the stellar population of the galaxy pairs. However, this requires the more dusty galaxies to have an intrinsically older and therefore redder stellar population than the less dusty galaxies, despite having the same observed  $\psi_S$ , metallicity, etc., which is opposite to the slight trend with inclination that we observe in the data.

It is possible that the steeper slopes are a result of a differential effect related to the distribution of dust around stars of different ages. In ordinary star-forming galaxies, younger (older) stars contribute a larger fraction of the blue (red) optical light. This is different from low-mass starburst or old elliptical galaxies, in which the majority of light at all wavelengths comes from young or old stars. If young, blue stars suffer greater dust extinction than old, red stars, then we will observe an apparently steeper attenuation curve in star-forming galaxies than the underlying extinction curve. This effect is the common explanation for the difference in attenuation observed in emission lines and galaxy continua (see Section 5.4). We observe that the slope is steeper in galaxies with significant bulges. This could occur if the older stellar population in the bulge is less obscured by dust than the younger stellar population in the disc. Slopes closer to the extinction curves observed in edge-on galaxies could arise as the disc obscures a greater fraction of the old stellar population in the bulge.

If the steeper slopes are a result of the relative geometry of stars and dust, we would expect a weaker effect in the smaller apertures where the light comes mainly from older stars in the bulge, especially in face-on galaxies: at  $0.35R_{\text{pet}}$ , we find  $s_{\text{opt}} = 1.07$  for  $b/a = 0.35$ , and  $1.31$  for  $b/a = 0.88$ . This is, respectively, 3 and 22 per cent smaller than the values for  $s_{\text{opt}}$  at  $0.9R_{\text{pet}}$ , qualitatively in agreement with the hypothesis that the steep curves arise due to a differential effect whereby different stellar populations are attenuated by different dust columns.

One final possibility is presented by radiative transfer models of dust in galaxies. These can also exhibit steeper optical attenuation curves than the input extinction curves, in the optically thin limit and with certain geometric configurations (Pierini et al. 2004; Tuffs et al. 2004), even before effects for different stellar populations are included. Ultimately, the cause for the steep optical slopes must be solved by comparison with such models. This is beyond the scope of this paper (see Chevallard et al., in preparation).

## 5.2 The slope of the attenuation curve in the NIR

In Fig. 5, we show the slope of the attenuation curve in the NIR, as a function of  $\psi_S$  and axial ratio. Within the errors, we find no significant overall deviation from the MW extinction curve with a slope of 1.6, and no clear trends with galaxy properties are evident. For the LMC and C00 curves, we find NIR slopes of 1.7, almost identical to the MW curve. The SMC-bar curve of Gordon et al. (2003) exhibits a strong bump in the NIR that prevents us from fitting a robust power-law slope. Inspection of the individual curves in Gordon et al. (2003) reveals that a significant deviation from a power-law slope is only evident in one out of the four stars that contribute to the average curve. We therefore conclude that this bump may result from photometric errors and small number statistics, and we therefore do not compare our results with the SMC-bar curve in the NIR wavelength regime.

The constancy of the NIR slope of extinction laws along multiple lines of sight to stars in the MW is an important feature of the MW extinction curve, implying a constant-size distribution of the largest particles throughout both diffuse and dense clouds of dust (Mathis 1990). The same value found here in external galaxies leads to the conclusion that the size distribution of the largest dust particles is universal. It additionally implies that the factors affecting the attenuation of light in galaxies (dust–star and global geometry, scattering into the line of sight) are unimportant at long wavelengths. Recent work by Stead & Hoare (2009) suggests a slightly steeper MW NIR slope of 2.14 by comparison of UKIDSS data with the Besançon Galactic model. If this is the case, this would instead

**Table 3.** Parameters of broken power-law fits to attenuation curves for each SDSS+UKIDSS sample (see equation 9). Measurements of the shape and amplitude of the attenuation curves are made from circular aperture photometry measured at 90 per cent of the  $r$ -band Petrosian radius. The line-to-continuum ratio is measured using a 1.76-arcsec-radius fixed angular aperture, to best match the emission-line measurement through the SDSS fibre. Note that the slopes and  $\tau$  ratios are fundamental quantities, whereas the  $\Delta\tau$  values are sample-dependent.

	$s_{\text{opt}}$	$s_{\text{nir}}$	$\lambda_c/\mu\text{m}$	$\Delta\tau_{\lambda_c}$	$\Delta\tau_K$	$\Delta\tau_{V,\text{cont}}$	$\frac{\Delta\tau_{V,\text{line}}}{\Delta\tau_{V,\text{cont}}}$ (3 arcsec)
$\mu^* < 3 \times 10^8$							
All galaxies	$1.02^{+0.05}_{-0.05}$	$1.54^{+0.33}_{-0.50}$	$0.95^{+0.02}_{-0.08}$	$0.10^{+0.01}_{-0.01}$	$0.03^{+0.01}_{-0.01}$	$0.18^{+0.01}_{-0.01}$	$2.56^{+0.10}_{-0.12}$
$-11.00 < \log(\psi_S/\text{yr}^{-1}) < -9.90$	$1.03^{+0.09}_{-0.09}$	$1.78^{+0.59}_{-0.37}$	$0.95^{+0.03}_{-0.00}$	$0.11^{+0.03}_{-0.03}$	$0.02^{+0.02}_{-0.01}$	$0.19^{+0.02}_{-0.02}$	$2.92^{+0.26}_{-0.35}$
$-9.90 < \log(\psi_S/\text{yr}^{-1}) < -9.75$	$1.16^{+0.07}_{-0.12}$	$2.61^{+0.89}_{-1.53}$	$0.71^{+0.03}_{-0.00}$	$0.11^{+0.01}_{-0.02}$	$0.00^{+0.02}_{-0.00}$	$0.15^{+0.02}_{-0.01}$	$2.71^{+0.17}_{-0.18}$
$-9.75 < \log(\psi_S/\text{yr}^{-1}) < -9.62$	$1.14^{+0.09}_{-0.09}$	$2.84^{+1.25}_{-1.22}$	$0.80^{+0.02}_{-0.00}$	$0.09^{+0.01}_{-0.02}$	$0.01^{+0.02}_{-0.01}$	$0.14^{+0.02}_{-0.01}$	$2.78^{+0.36}_{-0.29}$
$-9.62 < \log(\psi_S/\text{yr}^{-1}) < -9.46$	$1.12^{+0.07}_{-0.09}$	$1.96^{+0.50}_{-0.49}$	$0.94^{+0.03}_{-0.00}$	$0.09^{+0.01}_{-0.01}$	$0.02^{+0.01}_{-0.01}$	$0.17^{+0.02}_{-0.01}$	$2.71^{+0.18}_{-0.15}$
$-9.46 < \log(\psi_S/\text{yr}^{-1}) < -9.25$	$0.95^{+0.07}_{-0.13}$	$1.29^{+0.35}_{-0.36}$	$0.70^{+0.07}_{-0.21}$	$0.15^{+0.02}_{-0.03}$	$0.04^{+0.03}_{-0.01}$	$0.19^{+0.03}_{-0.02}$	$2.41^{+0.14}_{-0.17}$
$-9.25 < \log(\psi_S/\text{yr}^{-1}) < -7.90$	$1.04^{+0.12}_{-0.09}$	$1.83^{+0.41}_{-0.40}$	$0.70^{+0.04}_{-0.09}$	$0.14^{+0.02}_{-0.03}$	$0.01^{+0.03}_{-0.02}$	$0.17^{+0.03}_{-0.02}$	$2.08^{+0.22}_{-0.14}$
$0.0 < b/a < 0.4$	$0.91^{+0.06}_{-0.04}$	$1.86^{+0.50}_{-0.26}$	$0.96^{+0.02}_{-0.08}$	$0.16^{+0.01}_{-0.01}$	$0.03^{+0.01}_{-0.01}$	$0.27^{+0.01}_{-0.02}$	$2.01^{+0.15}_{-0.11}$
$0.4 < b/a < 0.6$	$0.97^{+0.10}_{-0.18}$	$0.92^{+1.38}_{-1.35}$	$0.95^{+0.08}_{-0.09}$	$0.11^{+0.01}_{-0.01}$	$0.05^{+0.04}_{-0.01}$	$0.19^{+0.03}_{-0.01}$	$3.15^{+0.23}_{-0.17}$
$0.6 < b/a < 0.8$	$1.12^{+0.12}_{-0.10}$	$1.29^{+0.50}_{-0.38}$	$0.70^{+0.07}_{-0.08}$	$0.11^{+0.01}_{-0.01}$	$0.02^{+0.02}_{-0.01}$	$0.14^{+0.02}_{-0.01}$	$3.45^{+0.29}_{-0.30}$
$0.8 < b/a < 1.0$	$1.25^{+0.08}_{-0.10}$	$2.14^{+0.87}_{-0.40}$	$0.72^{+0.00}_{-0.02}$	$0.07^{+0.01}_{-0.01}$	$0.01^{+0.01}_{-0.01}$	$0.10^{+0.01}_{-0.01}$	$3.74^{+0.30}_{-0.34}$
$\mu^* > 3 \times 10^8$							
All galaxies	$1.28^{+0.01}_{-0.01}$	$1.57^{+0.08}_{-0.07}$	$0.82^{+0.01}_{-0.01}$	$0.14^{+0.00}_{-0.00}$	$0.03^{+0.00}_{-0.00}$	$0.23^{+0.00}_{-0.01}$	$2.39^{+0.07}_{-0.06}$
$-11.00 < \log(\psi_S/\text{yr}^{-1}) < -9.90$	$1.19^{+0.06}_{-0.08}$	$1.78^{+0.50}_{-0.31}$	$0.96^{+0.00}_{-0.09}$	$0.11^{+0.01}_{-0.03}$	$0.03^{+0.01}_{-0.01}$	$0.21^{+0.02}_{-0.01}$	$2.72^{+0.17}_{-0.17}$
$-9.90 < \log(\psi_S/\text{yr}^{-1}) < -9.75$	$1.28^{+0.08}_{-0.08}$	$1.64^{+0.30}_{-0.17}$	$0.89^{+0.13}_{-0.00}$	$0.12^{+0.01}_{-0.02}$	$0.02^{+0.01}_{-0.01}$	$0.21^{+0.01}_{-0.02}$	$2.53^{+0.17}_{-0.17}$
$-9.75 < \log(\psi_S/\text{yr}^{-1}) < -9.62$	$1.42^{+0.10}_{-0.06}$	$1.74^{+0.37}_{-0.27}$	$0.70^{+0.04}_{-0.09}$	$0.15^{+0.01}_{-0.01}$	$0.03^{+0.01}_{-0.01}$	$0.21^{+0.02}_{-0.02}$	$2.62^{+0.15}_{-0.20}$
$-9.62 < \log(\psi_S/\text{yr}^{-1}) < -9.46$	$1.34^{+0.12}_{-0.04}$	$1.25^{+0.33}_{-0.17}$	$0.81^{+0.03}_{-0.10}$	$0.14^{+0.00}_{-0.01}$	$0.04^{+0.01}_{-0.01}$	$0.23^{+0.01}_{-0.03}$	$2.34^{+0.14}_{-0.15}$
$-9.46 < \log(\psi_S/\text{yr}^{-1}) < -7.90$	$1.37^{+0.06}_{-0.05}$	$1.72^{+0.30}_{-0.15}$	$0.85^{+0.09}_{-0.03}$	$0.15^{+0.01}_{-0.00}$	$0.03^{+0.01}_{-0.01}$	$0.26^{+0.01}_{-0.01}$	$1.97^{+0.12}_{-0.08}$
$0.0 < b/a < 0.4$	$1.10^{+0.05}_{-0.05}$	$1.70^{+0.29}_{-0.20}$	$1.00^{+0.04}_{-0.08}$	$0.14^{+0.01}_{-0.01}$	$0.04^{+0.01}_{-0.01}$	$0.28^{+0.01}_{-0.01}$	$2.06^{+0.10}_{-0.12}$
$0.4 < b/a < 0.6$	$1.27^{+0.04}_{-0.05}$	$1.51^{+0.11}_{-0.15}$	$0.83^{+0.02}_{-0.02}$	$0.14^{+0.00}_{-0.01}$	$0.03^{+0.01}_{-0.00}$	$0.24^{+0.01}_{-0.01}$	$2.30^{+0.15}_{-0.09}$
$0.6 < b/a < 0.8$	$1.39^{+0.06}_{-0.06}$	$1.31^{+0.21}_{-0.20}$	$0.85^{+0.13}_{-0.09}$	$0.11^{+0.03}_{-0.01}$	$0.03^{+0.01}_{-0.01}$	$0.21^{+0.02}_{-0.01}$	$2.58^{+0.19}_{-0.20}$
$0.8 < b/a < 1.0$	$1.59^{+0.08}_{-0.06}$	$2.59^{+0.32}_{-0.21}$	$1.00^{+0.00}_{-0.00}$	$0.06^{+0.01}_{-0.01}$	$0.01^{+0.01}_{-0.00}$	$0.15^{+0.01}_{-0.01}$	$2.79^{+0.20}_{-0.24}$
MW (CCM+OD)	1.06	1.6	0.82	$0.20^b$	$0.038^b$	$0.3^b$	–
C00	0.96	1.7	0.91	$0.18^b$	$0.034^b$	$0.3^b$	$2.08^a$
LMC	1.05	1.7	0.90	$0.17^b$	$0.020^b$	$0.3^b$	–
SMC bar <sup>c</sup>	1.2	–	–	$0.16^b$	–	$0.3^b$	–

<sup>a</sup>  $E(B - V)_{\text{stars}} = 0.44E(B - V)_{\text{gas}}$  (Calzetti 1997b, 2001) converted into a ratio of optical depths, assuming the emission-line attenuation curve from Wild et al. (2011).

<sup>b</sup> In the case of the MW, C00, LMC and SMC-bar curves, the  $\tau$  values are absolute and given for  $\tau_V = 0.3$  and  $\tau_K$  is given at a rest frame assuming  $z = 0.7$ .

<sup>c</sup> We are unable to reliably measure the NIR slope of the SMC-bar extinction curve (see Section 5.2).

imply some degree of flattening in the NIR attenuation curve of external galaxies. It is clear that further work on measuring the shape of extinction curves in the MW and local galaxies would be helpful to understand the dust distribution in more distant galaxies.

### 5.3 Radial gradients in total dust attenuation

In this section, we provide a more quantitative analysis of dust radial gradients than can be achieved by visual inspection of Figs 2 and 3. Because our methodology only provides a relative difference in dust content between the less and more dusty galaxies, we normalize the measured  $\Delta\tau_V$  values at all radii by the value at  $0.9R_{\text{pet}}$ . This then allows a direct comparison between samples. We measure  $\Delta\tau_V$  from the independent power-law fits to the dust curves at each different radius. It can be shown that, in the case where  $\tau_V(r)/\tau_V(0.9R_{\text{pet}})$  is the same, on average, for both the more and less dusty galaxies that make up the pairs in a particular sample, that is, within a particular

bin, the strength of the radial gradients is independent of the overall dust content, then  $\Delta\tau_V(r)/\Delta\tau_V(0.9R_{\text{pet}}) = \tau_V(r)/\tau_V(0.9R_{\text{pet}})$ . However, whether this is the case or not does not affect the identification of trends in which we are primarily interested.

Fig. 6 shows  $\Delta\tau_V$  measured within  $0.35$  and  $0.5R_{\text{pet}}$ , relative to  $\Delta\tau_V$  measured at  $0.9R_{\text{pet}}$ . In this section only, we fix the NIR slope to 1.6 during the fits, because for small apertures, the errors increase substantially on the measured NIR slope. In the left-hand panels, we see a strong trend in the strength of radial gradients with  $\psi_S$ : gradients are significantly larger in high- $\psi_S$  galaxies than in low- $\psi_S$  galaxies. In the low- $\mu^*$  sample, the trend appears to flatten above  $\psi_S \sim -9.5$ . In the right-hand panels, we see no strong trends in the strength of the radial gradients with axial ratio, although the slightly weaker radial gradients in very inclined galaxies are likely a real feature caused by large optical depths. It is notable that both the high- and low- $\mu^*$  samples show the same strength of radial gradient. Averaging over all bins in  $b/a$ , we find that the dust optical depth

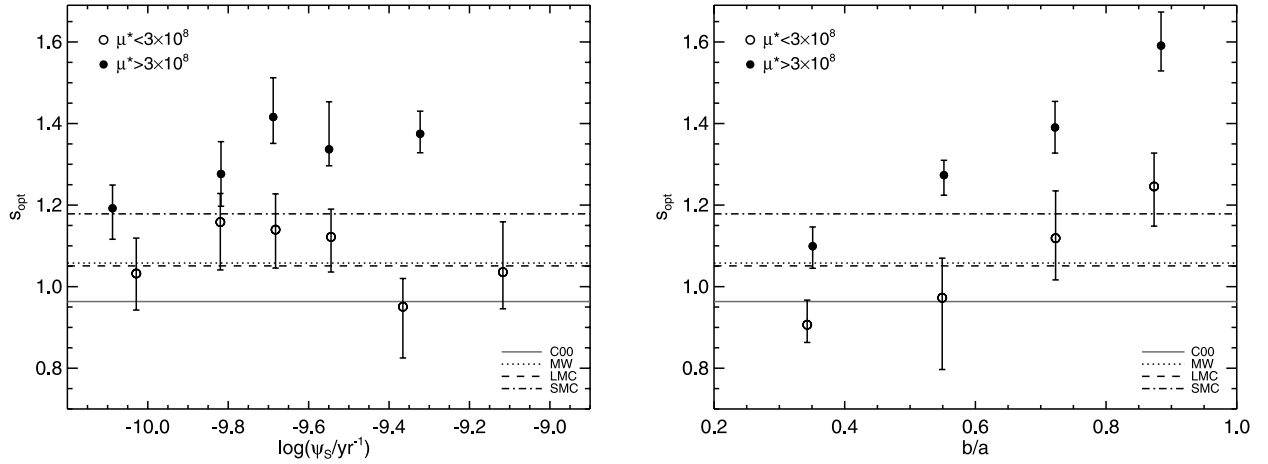


**Figure 4.** Power-law slope of the attenuation curve in the optical wavelength range, as a function of  $\psi_S$  (left-hand panel) and axial ratio (right-hand panel), for low- $\mu^*$  (open circles) and high- $\mu^*$  (filled circles) galaxies. The horizontal lines indicate the equivalent slopes for the MW (dotted line), C00 (grey, solid line), LMC (dashed line) and SMC-bar (dot-dashed line) curves.

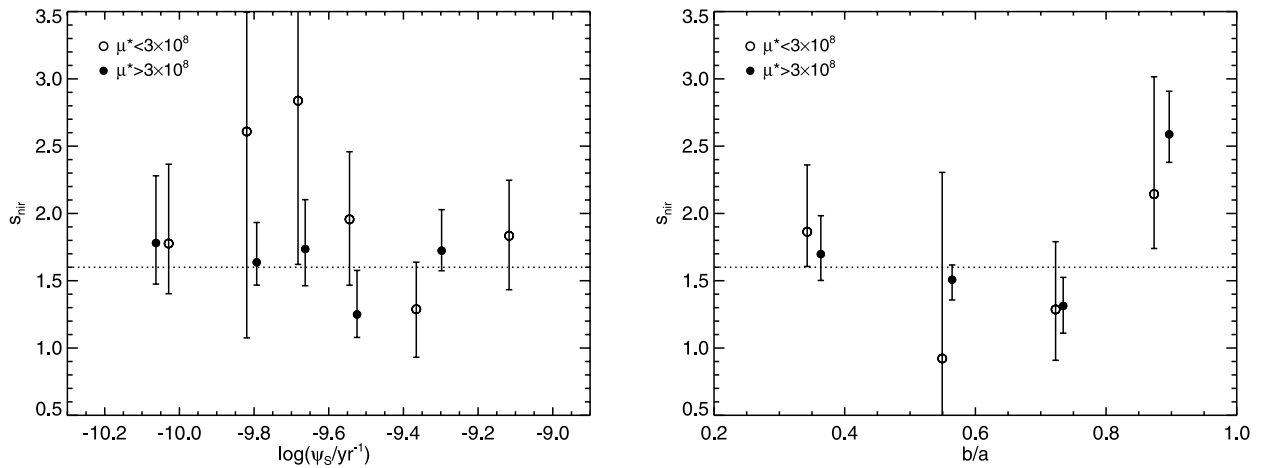


**Figure 5.** Power-law slope of the attenuation curve in the NIR wavelength range, as a function of  $\psi_S$  (left-hand panel) and observed axial ratio (right-hand panel), for low- $\mu^*$  (open circles) and high- $\mu^*$  (filled circles) galaxies. For clarity, the high- $\mu^*$  symbols have been offset slightly to the right-hand side. The dotted line indicates the equivalent slope for the MW extinction curve.

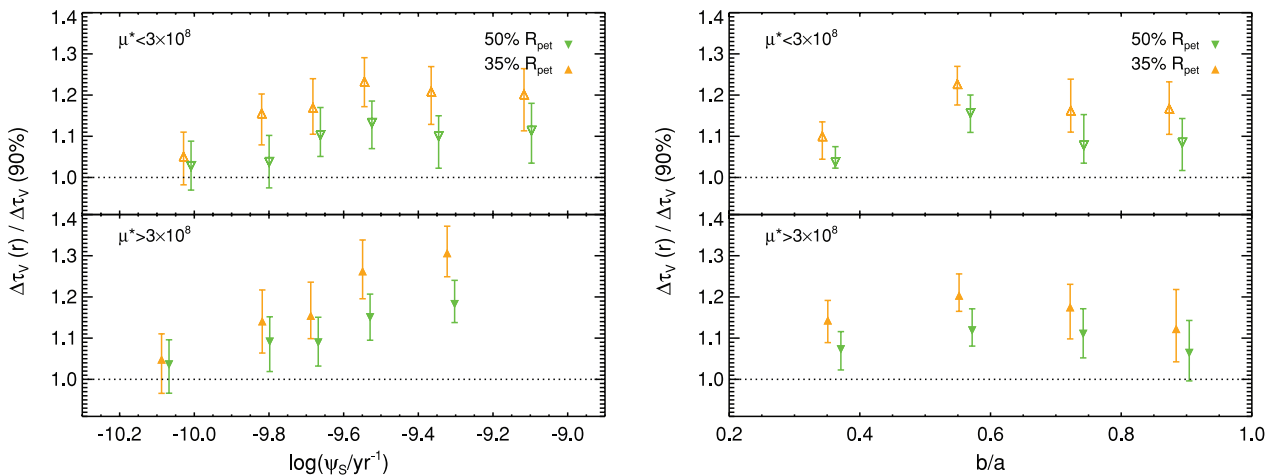


**Figure 6.** Radial gradients in continuum optical depth. Relative optical depth at  $5500 \text{ \AA}$  towards stars contained within 35 per cent (yellow, upward triangle) and 50 per cent (green, downward triangle) of the Petrosian radius of the galaxies, relative to the optical depth measured at 90 per cent of the Petrosian radius, as a function of  $\psi_S$  (left-hand panel) and axial ratio (right-hand panel). The top (bottom) part of each panel shows the results for low- $\mu^*$  (high- $\mu^*$ ) galaxies.

within  $0.35$  and  $0.5R_{\text{pet}}$  is  $1.16$  and  $1.09$  times that within  $0.9R_{\text{pet}}$ , for both samples. This indicates that the presence of a bulge does not affect the strength of radial gradients in dust distribution.

Measuring the trends of radial gradient strength with  $\psi_S$  is important in understanding the production and destruction of dust relative to ongoing or past star formation. The dust gradients reported here, and elsewhere in the literature for spatially resolved studies of small numbers of local galaxies (e.g. Muñoz-Mateos et al. 2009), are presumably related to metallicity gradients in spiral discs. However, because our  $\psi_S$  measurements relate strictly to the central  $3$  arcsec of the galaxies, and the scale of star formation episodes is known to depend on the rate of star formation (Kennicutt 1998), spatially resolved information on SFRs is required before firm conclusions can be drawn. Suitable spatially resolved spectral studies of metallicity, dust and star formation gradients in large numbers of disc galaxies have yet to be undertaken.

#### 5.4 Dust attenuation of nebular emission lines versus stellar continua

All of the galaxies in our sample have both  $H\alpha$  and  $H\beta$  line measurements which, until now, we have used only to derive relative dust content. Here we make use of the line fluxes to compare the dust attenuation suffered by the nebular emission lines and stellar continuum. The SDSS spectra are taken using a  $3$ -arcsec-diameter fibre, meaning that smaller galaxies, and those at higher redshift, have a larger fraction of their total light included in the spectrum. In our sample, the median projected fibre radius is around  $0.35R_{\text{pet}}$ , but with a wide distribution. In light of the radial gradients measured in the previous section, this fixed angular aperture restricts the extent to which we can compare dust attenuation of lines and continua in our sample. To provide the best comparison, in this section only, we measure the attenuation curves using a fixed  $1.76$ -arcsec-radius angular aperture (the curves are shown as the dotted lines in Figs 2 and 3). This is slightly larger than the  $1.5$ -arcsec-radius aperture of the fibre; however, the spectra are taken in worse seeing conditions than the imaging, and flux measurements at  $1.76$  arcsec are provided in the SDSS catalogue, thus preventing any small errors introduced by the interpolation of the radial flux curves.

Using the same formalism as for dust attenuation of the stellar continuum (Section 2.1), the amount of dust attenuation of nebular emission lines in more dusty relative to less dusty galaxies is given by

$$\Delta\tau_{\lambda,\text{line}} = \Delta\tau_{V,\text{line}} Q_{\lambda,\text{line}}, \quad (10)$$

where  $Q_{\lambda,\text{line}}$  describes the shape of the attenuation curve applicable for emission lines. Wild et al. (2011) compared mid-IR and optical emission-line strengths to show that a two-component model (Charlot & Fall 2000), with diffuse dust accounting for a fraction ( $\mu$ ) of the optical depth at  $5500 \text{ \AA}$ , and denser birth-cloud dust accounting for the remainder, is consistent with the emission-line ratios observed in a wide range of galaxy types:

$$Q_{\lambda,\text{line}} = (1 - \mu)(\lambda/\lambda_V)^{-m} + \mu(\lambda/\lambda_V)^{-n}. \quad (11)$$

In Wild et al. (2011), we measured  $\mu = 0.4$ , for the case where  $m = 1.3$  and  $n = 0.7$ . Ultimately, the slopes  $n$  and  $m$  may also be measured through comparison between the attenuation curves measured in this paper and models. However, for the purposes of this paper, it is sufficient to know that an accurate  $\tau_{V,\text{line}}$  is obtained from the Balmer emission-line ratios, as shown by Wild et al. (2011). Equation (11) leads to the dust optical depth for emission lines, as a function of wavelength and ratio of  $H\alpha$  to  $H\beta$  luminosity:

$$\Delta\tau_{\lambda,\text{line}} = \frac{\ln\left(\frac{f_{H\beta,1}}{f_{H\beta,2}}\right) - \ln\left(\frac{f_{H\alpha,1}}{f_{H\alpha,2}}\right)}{Q_{H\beta,\text{line}} - Q_{H\alpha,\text{line}}} Q_{\lambda,\text{line}}, \quad (12)$$

where  $Q_{H\beta,\text{line}} - Q_{H\alpha,\text{line}} = 0.310$ .

In Fig. 7, we show the ratio of the dust optical depth in the emission lines to the optical depth in the stellar continuum as a function of  $\psi_S$  and axial ratio. In both samples, we find a strong trend with  $\psi_S$  (left-hand panel), with both low- and high- $\mu^*$  galaxies having a line-to-continuum attenuation ratio  $50$  per cent higher at lower  $\psi_S$  than at high  $\psi_S$ . There is also a strong trend with axial ratio, with high-axial-ratio galaxies having a higher line-to-continuum attenuation ratio than low-axial-ratio galaxies. Similar trends with axial ratio are observed in both low- and high- $\mu^*$  galaxies, but low- $\mu^*$  galaxies are generally offset to higher overall ratios.

These trends can be interpreted in terms of the two different dust components in galaxies (diffuse versus birth-cloud dust as described

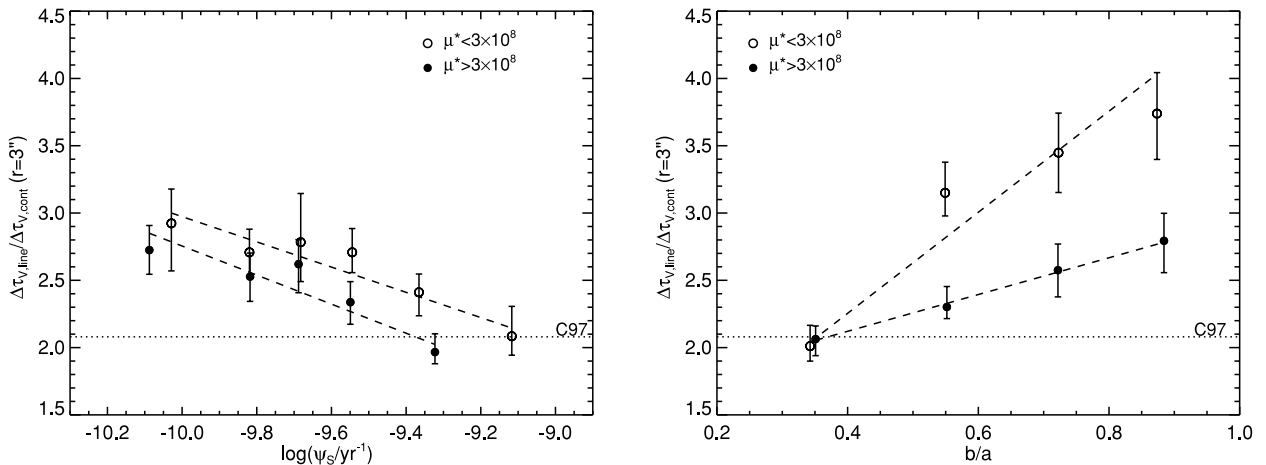


**Figure 7.** Dust optical depth towards the Balmer emission lines, relative to the dust optical depth in the continuum at  $5500 \text{ \AA}$ , as a function of  $\psi_S$  (left-hand panel) and axial ratio (right-hand panel). Unlike previous figures, the optical depth in the continuum has been measured using a fixed angular aperture of radius  $1.76$  arcsec to approximately match the emission-line measurements which are obtained through an optical fibre with a  $1.5$ -arcsec-radius aperture in generally worse seeing conditions. The dotted line indicates the line-to-continuum optical depth ratio from Calzetti (1997b), assuming the same attenuation curve for the emission lines as used in our analysis (equation 11). The dashed lines are fitted to the data points and are described in the text.

above), with young and old stars suffering different attenuation. The difference between the high- and low- $\mu^*$  galaxies may relate to the lower overall metallicity of the diffuse ISM in the latter sample, leading to lower diffuse dust contents. The slightly non-linear trend with  $b/a$  for the low- $\mu^*$  galaxies follows qualitatively that expected for a dust disc of finite thickness, with the optical depth of the diffuse ISM varying with the ratio of scaleheight to scalelength. One further point of note is the equal ratio found at high  $\psi_S$  and low  $b/a$ . Such a coincidence of ratios is not expected a priori, as the former property is intrinsic to the galaxies and the latter is observer-dependent. This may indicate the true limit of optical observations, where significant numbers of sightlines are lost due to high column densities of diffuse dust, either due to long path-lengths or high dust contents. Such a ‘skin’ effect would lead to only the stars closest to the observer contributing to the observed integrated light. We will return to all these points in Section 7.

As in the case of the radial gradients presented in the previous subsection, in the case where  $\tau_{V,\text{line}}/\tau_{V,\text{cont}}$  is independent of the overall dust content, it can be shown that  $\Delta\tau_{V,\text{line}}/\Delta\tau_{V,\text{cont}} = \tau_{V,\text{line}}/\tau_{V,\text{cont}}$ . In Appendix A, Fig. A1 shows that this is indeed the case, and therefore we can write (dashed lines in Fig. 7)

$$\frac{\tau_{V,\text{line}}}{\tau_{V,\text{cont}}} = 0.75(\pm 0.2) + 3.8(\pm 0.6)b/a \quad (\text{low } \mu^*) \quad (13)$$

$$= 1.6(\pm 0.2) + 1.4(\pm 0.4)b/a \quad (\text{high } \mu^*) \quad (14)$$

and

$$\frac{\tau_{V,\text{line}}}{\tau_{V,\text{cont}}} = -6.4(\pm 2.6) - 0.9(\pm 0.3)\psi^* \quad (\text{low } \mu^*) \quad (15)$$

$$= -8.0(\pm 2.6) - 1.1(\pm 0.3)\psi^* \quad (\text{high } \mu^*) \quad (16)$$

Calzetti (1997b) measured the same quantity for starburst galaxies, finding  $E(B - V)_{\text{stars}} = 0.44E(B - V)_{\text{line}}$ . For the emission-line attenuation curve given in equation (11), this corresponds to  $\tau_{V,\text{line}}/\tau_{V,\text{cont}} = 0.44R_{V,\text{line}}/R_{V,\text{cont}} = 2.08$ . This is shown as a dotted line in Fig. 7, which is close to the value measured for high- $\psi_S$  galaxies in our sample.

### 5.5 The slope of the attenuation curve in the UV

In the previous subsections, we used the larger SDSS+UKIDSS galaxy sample. We now turn on to the analysis of the subsample of galaxies with UV fluxes, repeating the pair-matching procedure from the start. The results of the optical–NIR fits remain the same as in the full sample, albeit with larger errors resulting from the smaller sample sizes. In this section, we define the slopes for FUV–NUV and FUV– $u$  as

$$s' = -\frac{\log(-\mathcal{T}_{\lambda_1}) - \log(-\mathcal{T}_{\lambda_2})}{\log \lambda_1 - \log \lambda_2}. \quad (17)$$

Note that  $s'$  would only be equivalent to the power-law slopes ( $s$ ) of the previous subsections (equation 9), if the attenuation in the  $K$  band ( $\Delta\tau_K$ ) were equal to zero. Due to the smaller data set used in this sample, we quote  $s'$  rather than  $s$  in order to provide measurements that are independent of the optical–NIR attenuation curves. At these short wavelengths,  $s$  and  $s'$  are not significantly different. We test this by measuring both  $s$  and  $s'$  from the literature dust curves, normalizing at the rest-frame wavelength of the  $K$  band at the median redshift of our samples. We find  $s' - s \sim 0.03$ , well within our measurement errors.

To quantify the influence of the strong bump in the MW extinction curve on broad-band attenuation measurements, we convolve the

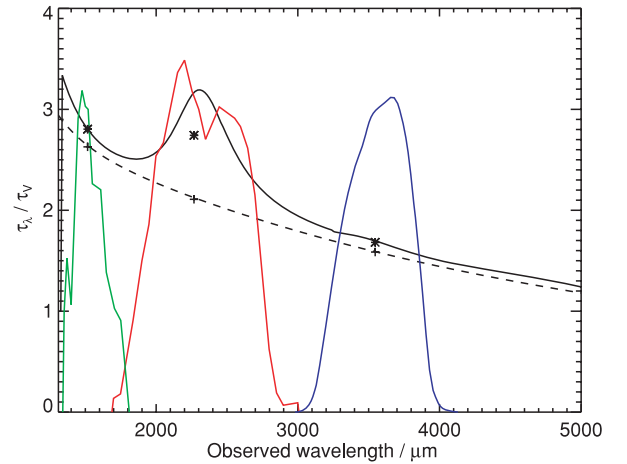


**Figure 8.** The MW (solid line) and C00 (dashed line) attenuation curves in the UV–optical wavelength range. Overplotted are the UV filter response functions from the *GALEX* and the SDSS  $u$  band. The stars (MW) and crosses (C00) indicate the attenuation in each of these bands after convolution with the filter functions.

comparison dust curves with the filter response functions (see also the discussion in Section 2.2). Fig. 8 shows the MW and C00 dust curves in the UV, with the FUV, NUV and  $u$ -band filters overplotted. The stars/crosses indicate the filter-averaged attenuation of each curve in the three bands: clearly the filter-averaged attenuation in the *GALEX* NUV band for the MW curve is less than the actual attenuation at 2175 Å. This figure also shows how the slope between the FUV and NUV bands, at median rest-frame wavelengths of 1430 and 2138 Å, probes the depth of the 2175-Å dust feature, whereas the slope between the FUV and  $u$  bands measures the shape of the underlying dust continuum.

Table 4 gives the measured UV slopes for all samples, together with comparison values for dust curves in the literature. In the top panels of Fig. 9, we find that  $s'_{\text{FUV}-u}$  is slightly higher on average in the high- $\mu^*$  samples than the low- $\mu^*$  samples. The two samples straddle the value measured for the MW and C00 curves ( $s'_{\text{FUV}-u} = 0.6$  in both cases). There is some evidence that the UV attenuation curve steepens with increasing  $b/a$  in the high- $\mu^*$  sample, and there is a possible steepening of slope with  $\psi_S$  in the low- $\mu^*$  sample.

In the bottom panels of Fig. 9, we find that  $s'_{\text{FUV}-\text{NUV}}$  generally lies between the values measured from the MW and C00 curves. The MW extinction curve, with a strong 2175-Å dust bump, has  $s'_{\text{FUV}-\text{NUV}} = 0.06$ , whereas the C00 attenuation curve with no dust bump has  $s'_{\text{FUV}-\text{NUV}} = 0.58$ , similar to the global (FUV– $u$ ) slope of this curve ( $s'_{\text{FUV}-u} = 0.62$ ). For the high- $\mu^*$  galaxies, we find that the bump strength increases strongly with increasing  $b/a$ , ranging from close to the C00 curve in face-on galaxies to close the MW curve in edge-on galaxies. The same trend is not observed in the low- $\mu^*$  galaxies. A weaker trend of increasing bump strength with decreasing  $\psi_S$  may reconcile our results with the weak bump observed in starburst galaxies by C00.

The 2175-Å feature is widely believed to be a pure absorption feature, with its strength in extinction curves varying depending on the chemical composition and/or physical environment of the dust grains (Draine 2003). In attenuation curves, the balance of scattering versus absorption could affect the strength of the feature. The similarity in overall strength between the low- and high- $\mu^*$  galaxies, which have different average metallicities, could imply that much lower metallicities than are present in our sample are required to

**Table 4.** Slopes of the UV attenuation curves for each SDSS+UKIDSS+GALEX sample (see equation 17), and comparison literature curves.

	$S'_{\text{FUV-NUV}}$	$S'_{\text{FUV-u}}$
$\mu^* < 3 \times 10^8$		
All galaxies	$0.28^{+0.04}_{-0.03}$	$0.54^{+0.02}_{-0.03}$
$-11.00 < \log(\psi_S/\text{yr}^{-1}) < -9.90$	$0.09^{+0.14}_{-0.12}$	$0.36^{+0.09}_{-0.08}$
$-9.90 < \log(\psi_S/\text{yr}^{-1}) < -9.75$	$0.26^{+0.17}_{-0.11}$	$0.44^{+0.08}_{-0.08}$
$-9.75 < \log(\psi_S/\text{yr}^{-1}) < -9.62$	$0.47^{+0.14}_{-0.15}$	$0.68^{+0.10}_{-0.07}$
$-9.62 < \log(\psi_S/\text{yr}^{-1}) < -9.46$	$0.23^{+0.09}_{-0.08}$	$0.45^{+0.07}_{-0.06}$
$-9.46 < \log(\psi_S/\text{yr}^{-1}) < -9.25$	$0.26^{+0.08}_{-0.09}$	$0.57^{+0.07}_{-0.06}$
$-9.25 < \log(\psi_S/\text{yr}^{-1}) < -7.90$	$0.41^{+0.11}_{-0.11}$	$0.65^{+0.07}_{-0.06}$
$0.0 < b/a < 0.4$	$0.30^{+0.06}_{-0.08}$	$0.55^{+0.05}_{-0.05}$
$0.4 < b/a < 0.6$	$0.30^{+0.06}_{-0.08}$	$0.56^{+0.06}_{-0.04}$
$0.6 < b/a < 0.8$	$0.19^{+0.12}_{-0.08}$	$0.53^{+0.08}_{-0.06}$
$0.8 < b/a < 1.0$	$0.33^{+0.10}_{-0.12}$	$0.53^{+0.08}_{-0.08}$
$\mu^* > 3 \times 10^8$		
All galaxies	$0.32^{+0.04}_{-0.05}$	$0.74^{+0.03}_{-0.02}$
$-11.00 < \log(\psi_S/\text{yr}^{-1}) < -9.90$	$0.22^{+0.10}_{-0.09}$	$0.88^{+0.08}_{-0.07}$
$-9.90 < \log(\psi_S/\text{yr}^{-1}) < -9.75$	$0.21^{+0.15}_{-0.13}$	$0.66^{+0.10}_{-0.08}$
$-9.75 < \log(\psi_S/\text{yr}^{-1}) < -9.62$	$0.30^{+0.18}_{-0.12}$	$0.73^{+0.09}_{-0.10}$
$-9.62 < \log(\psi_S/\text{yr}^{-1}) < -9.46$	$0.39^{+0.10}_{-0.11}$	$0.72^{+0.07}_{-0.07}$
$-9.46 < \log(\psi_S/\text{yr}^{-1}) < -7.90$	$0.29^{+0.10}_{-0.09}$	$0.67^{+0.06}_{-0.05}$
$0.0 < b/a < 0.4$	$0.07^{+0.11}_{-0.09}$	$0.67^{+0.07}_{-0.08}$
$0.4 < b/a < 0.6$	$0.23^{+0.10}_{-0.08}$	$0.64^{+0.06}_{-0.06}$
$0.6 < b/a < 0.8$	$0.48^{+0.10}_{-0.10}$	$0.78^{+0.06}_{-0.05}$
$0.8 < b/a < 1.0$	$0.56^{+0.09}_{-0.11}$	$0.88^{+0.08}_{-0.05}$
MW (CCM+OD)	0.06	0.64
C00	0.58	0.62
LMC	0.27	0.71
SMC bar <sup>c</sup>	1.24	1.24

reduce the strength of the feature through chemical composition effects. The samples studied here are dominated by luminous and relatively massive galaxies. The C00 curve is well known for the lack of the 2175-Å feature, which may be due to dust grain destruction in the extreme physical environment. Again, although there is a hint in the data that the strength of the 2175-Å feature weakens with increasing  $\psi_S$ , the samples studied here are dominated by ordinary star-forming galaxies, not extreme starbursts.

The trend with axial ratio in the high- $\mu^*$  galaxies is interesting, as is the fact that the same trend is not seen in the low- $\mu^*$  galaxies. The lack of the overall difference in strength between the high- and low- $\mu^*$  samples implies that metallicity effects are not important here, which leaves the possibility of geometric effects. If dust is distributed uniformly with the stars, then by increasing the inclination of the galaxy, the amount of interstellar dust that starlight passes through on its way to the observer increases, which will increase the optical depth of absorption by the grains responsible for the 2175-Å feature. However, in the case of high- $\mu^*$  galaxies, which have significant bulges, the axial ratio is not as cleanly linked to inclination as in the case of low- $\mu^*$  galaxies. This makes our results difficult to interpret without further image decomposition that is not possible with GALEX data.

We conclude that a 2175-Å dust feature is present in most types of luminous galaxies, except possibly at high  $\psi_S$ , but its observed strength in attenuation curves can be modified by geometric effects. How these geometric effects act will require better spatially resolved observations and more detailed evaluation of dust models.

The implications of a significant 2175-Å dust feature extend beyond interest in the composition of dust grains, as it impacts significantly the observed UV spectral slope of galaxies (see also Burgarella et al. 2005), and thus estimates of the SFR density at high redshift (Meurer, Heckman & Calzetti 1999; Bouwens et al. 2009), and the metallicity and dust contents of high-redshift galaxies (Meurer et al. 1997; Bouwens et al. 2010; Dunlop et al. 2011). Predictions for the exact strength of the effect are difficult, given the wide variety of bands used to measure the UV spectral slope (commonly referred to as  $\beta$ ) and the lack of constraints on the stellar population of high-redshift galaxies. However, when the reddest band used to measure  $\beta$  lies close to 2175 Å as in Bouwens et al. (2010), incorrectly assuming a dust curve with no 2175-Å feature would lead to an underestimation of the amount of dust, leading to the incorrect conclusion that the stellar populations are extremely metal poor.

## 6 GLOBAL FIT OF THE DUST ATTENUATION CURVE

In the previous section, we used a combination of a parametrized fit and direct colour measurements to study the shape of the attenuation curves for independent galaxy samples binned by  $\psi_S$  and axial ratio. Parametrized fits of binned samples are important for robustly identifying systematic changes, but they do not provide an ‘attenuation law’ that can be used at all wavelengths in all data sets. In this section, we provide an empirically derived curve to describe the attenuation by dust at arbitrary wavelength, as a function of  $\psi_S$  and axial ratio, suitable for any observational data set. Where  $\psi_S$  and axial ratio are unknown, and no informed guess can be made, the ‘typical’ curve may be defined at the central points of  $\psi_S \sim -9.5$  and  $b/a \sim 0.6$ .

In this section, the data are not binned in  $\psi_S$  or  $b/a$ , so that each galaxy pair can be included at its rest-frame wavelength, and a smooth function with  $\psi_S$  and  $b/a$  can be derived. We use a multiple smoothly broken power law to describe the shape of the curve (Guidorzi et al. 2009).

In order to derive an average attenuation curve shape ( $Q_\lambda$ ) without prior binning of the data, we require an estimate of the optical depth in the continuum ( $\Delta\tau_{V,\text{cont}}$ ) for each pair, a quantity not known a priori. We therefore use the emission-line optical depth, taking into account the variation in line-to-continuum dust opacity ( $\Delta\tau_{V,\text{line}}/\Delta\tau_{V,\text{cont}}$ ) with  $\psi_S$  and  $b/a$  observed in Section 5.4, and the radial gradients in overall dust content observed in Section 5.3.

With only two broad bands in the UV, an accurate description of the 2175-Å region of the attenuation curve is not possible. While there is a definite change in slope of the curves, indicative of the 2175-Å feature observed along most lines of sight in the MW, we are unable to constrain the precise shape of this feature. We have therefore chosen to define a break in the attenuation curve at the central wavelength of the feature observed in the MW, but interpolate smoothly over the broad-band observations. This will not cause significant errors in the correction of broad-band fluxes for dust attenuation. However, when using our empirical curve to correct spectral observations, or narrow-band fluxes, readers should be aware of the limitations of our observations.

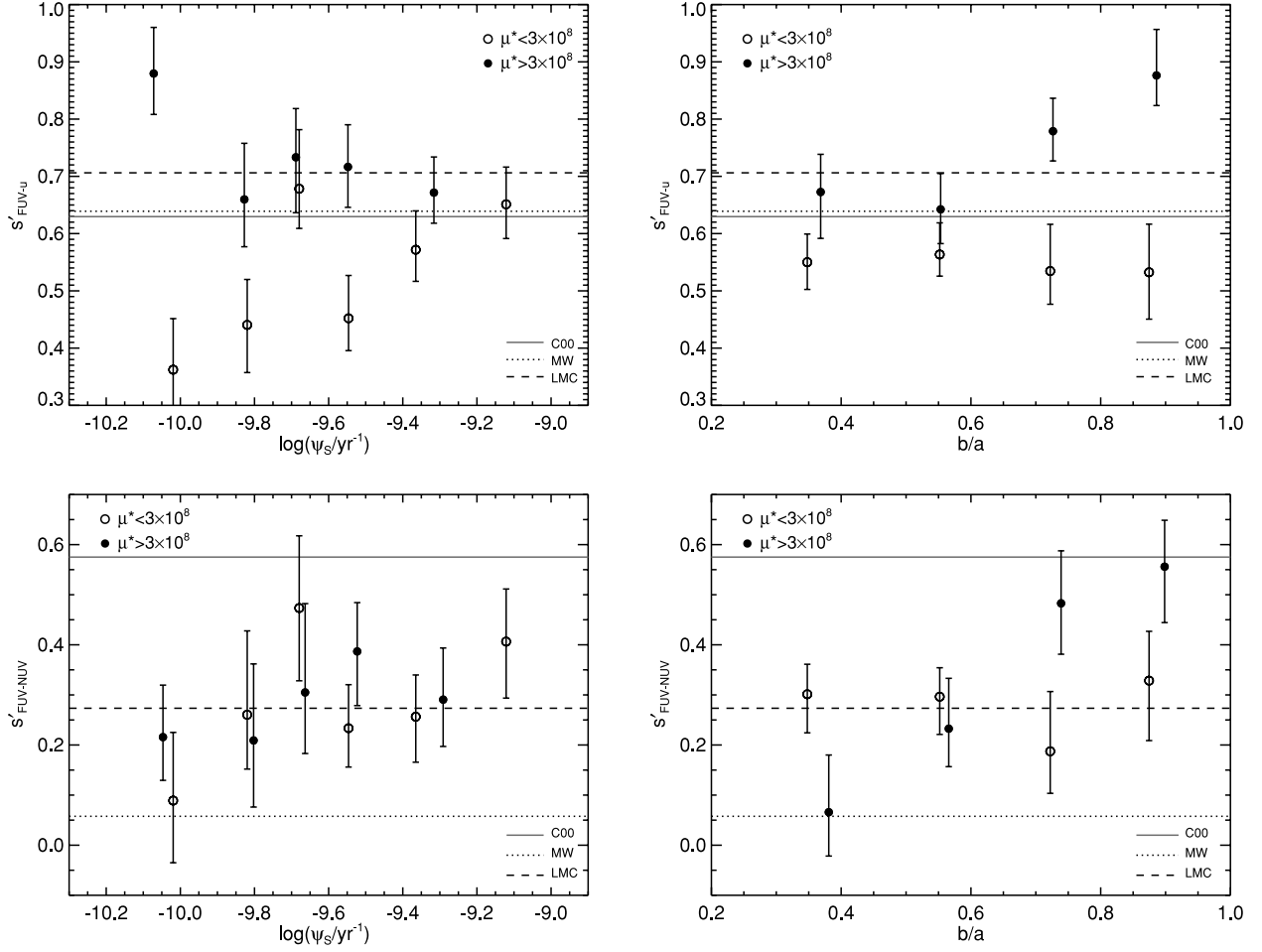


**Figure 9.** Power-law slope of the attenuation curves in the UV wavelength range, as a function of  $\psi_S$  (left-hand panels) and observed axial ratio (right-hand panels). In the top panels, we plot FUV– $u$ -band slope. The lower panels show the FUV–NUV slope. For clarity in the lower panels, the high- $\mu^*$  symbols have been offset slightly to the right-hand side. The horizontal lines mark the corresponding slopes for the MW (dotted line), C00 (grey, solid line), LMC (dashed line) and SMC-bar (dot-dashed line) curves after convolving with the filter response functions. The FUV– $u$  and FUV–NUV slopes of the SMC-bar extinction curve are 1.24, which is beyond the axis range.

The curve is composed of four power-law functions with exponents  $s_{[1-4]}$  smoothly joined with a smoothness parameter  $n$ . We define the position of the three break points ( $\lambda_{b[1-3],\text{eff}}$ ) at 0.2175, 0.3 and 0.8  $\mu\text{m}$ , respectively. The first is motivated by the central position of the dust bump in the MW curve. The second break point is positioned to produce a smooth transition between the steeper optical and shallower NUV slopes observed. The final break position is motivated by the results of our parametrized fits in Section 5. The sampling of the curves is too sparse to fit for the smoothness parameter  $n$ , and therefore we fix this to be 20 which results in a sufficiently smooth curve.

Following the formalism set out in Section 2.2, the shape of the attenuation curve is given by

$$Q_\lambda = \frac{1}{N} \left[ \left( \frac{\lambda}{\lambda_{b1}} \right)^{n s_1} + \left( \frac{\lambda}{\lambda_{b1}} \right)^{n s_2} + \left( \frac{\lambda}{\lambda_{b2}} \right)^{n s_3} + \left( \frac{\lambda}{\lambda_{b3}} \right)^{n s_4} \right]^{-1/n}, \quad (18)$$

where  $N$  is the normalization, defined such that the curve is unity at 5500  $\text{\AA}$ ;  $Q_V = 1$ ;  $n = 20$  defines the smoothness of the breaks. Note that due to the smoothing, the exponents of equation (18) are not all trivially related to the slopes measured in the previous section.

The effective positions of the break points are converted into the  $\lambda_{b[1-3]}$  values according to

$$\lambda_{b1} = \lambda_{b1,\text{eff}}, \quad (19)$$

$$\lambda_{b2} = \left[ \frac{\lambda_{b1}^{s_2}}{(\lambda_{b2,\text{eff}})^{s_2-s_3}} \right]^{1/s_3}, \quad (20)$$

$$\lambda_{b3} = \left[ \frac{\lambda_{b2}^{s_3}}{(\lambda_{b3,\text{eff}})^{s_3-s_4}} \right]^{1/s_4}, \quad (21)$$

with the effective positions of the breaks as motivated above.

The power-law slopes are allowed to vary with both axial ratio and  $\psi_S$  according to simple linear functions

$$s_1 = c_1 + c_2(b/a)_c + c_3(\psi_c), \quad (22)$$

$$s_2 = c_4 + c_5(b/a)_c + c_6(\psi_c), \quad (23)$$

$$s_3 = c_7 + c_8(b/a)_c + c_9(\psi_c), \quad (24)$$

$$s_4 = 1.6, \quad (25)$$

**Table 5.** Fitted constants for equation (18), which define the shape of the dust attenuation curve as a function of  $\psi_S$  and axial ratio.

Sample	$c_1$	$c_2$	$c_3$	$c_4$	$c_5$	$c_6$	$c_7$	$c_8$	$c_9$
$\mu^* < 3 \times 10^8$	0.15	0.00	0.20	0.70	0.00	0.40	1.10	0.40	-0.10
$\mu^* > 3 \times 10^8$	0.20	0.90	0.10	1.10	0.30	-0.20	1.30	0.60	0.10

where  $(b/a)_c = (b/a) - 0.6$  and  $\psi_c = \psi_S + 9.5$ . The functions are valid in the primary parameter ranges covered by the binned samples studied in this paper:  $0.3 < b/a < 0.9$  and  $-10.2 < \psi_S < -9.3$  for high  $\mu^*$  and  $-10.0 < \psi_S < -9.1$  for low  $\mu^*$ , and should not be extrapolated beyond these values. For galaxies outside these ranges, the functions could be calculated at the minimal or maximal extent of the range probed in our samples. The free parameters for high- and low- $\mu^*$  galaxies are provided in Table 5.

Fig. 10 shows the shape of the attenuation curves ( $Q_\lambda$ ) for different values of  $\psi_S$  and axial ratio. Fig. 11 compares the observed attenuation in our binned galaxy samples to the appropriate empirical curves for the median  $\psi_S$  and axial ratio of each sample. Overall, the agreement is excellent, with no trend in residuals with either parameter.

### 6.1 Comparison with other curves

In Fig. 12, we compare the dust curves derived here to the MW and C00 dust curves, for galaxies with  $\psi_S = -9.5$  and  $b/a = 0.6$ . For a galaxy with attenuation in the stellar continua of  $A_V = 1$ , the y-axis represents the difference in attenuation in magnitudes. The very steep attenuation in the blue found for the high- $\mu^*$  galaxies is evident here, as is the strong 2175-Å feature compared to the C00 curve. For the low- $\mu^*$  galaxies, the attenuation is almost indistinguishable from C00 redwards of 5500 Å, although the curves differ substantially in the blue, and the lack of a 2175-Å feature in the C00 curve is again evident. However, it is clear that for the low- $\mu^*$  galaxies, the feature is not as strong as in the MW.

A complete dust attenuation curve is built from the shape ( $Q_\lambda$ ), and the normalization, that is, the amount of dust attenuation suffered by the *continuum* at 5500 Å ( $\tau_V$ ).<sup>10</sup> The most appropriate estimator for  $\tau_V$  will depend on the particular data set. If the Balmer emission lines are used, then equations (13) and (15) provide the conversion between  $\tau_{V,\text{line}}$  and  $\tau_{V,\text{cont}}$  when the Balmer emission lines and continuum measurements are made within the same aperture. This is the best estimate possible with the SDSS data, but it assumes that the ratio measured within a 3-arcsec-diameter fibre is representative of the entire galaxy. Other possible estimations of  $\tau_V$  could come from the measurement of the dust emission in the FIR (da Cunha, Charlot & Elbaz 2008), or depth of the mid-IR silicate absorption feature (Wild et al. 2011).

## 7 DISCUSSION AND CONCLUSIONS

Our main results are as follows:

(i) *NIR slope.* The slope of the attenuation curve in the NIR is consistent with that measured for the MW extinction curve ( $\sim 1.6$ )

for all types of galaxies, irrespective of  $\psi_S$ , inclination angle or the presence or absence of a bulge.

(ii) *Optical/UV slope.* We find significant trends in the optical/UV slope of the attenuation curve with galaxy properties. The high- $\mu^*$  galaxies show a steeper blue/UV slope than the low- $\mu^*$  galaxies and the average MW extinction curve. A flattening of the slope with increasing inclination is evident in both the high- and low- $\mu^*$  galaxies. There is no trend in optical slope with total optical depth.

(iii) *2175-Å feature.* Most samples of galaxies exhibit a discontinuity in the UV attenuation curve that is suggestive of a 2175-Å dust feature at a level that is slightly weaker than seen in the MW. In the high- $\mu^*$  galaxies, the strength of the feature varies with axial ratio, from as strong as that observed in the MW extinction curve at low axial ratios to undetected at high axial ratios. There is some evidence that the bump weakens with increasing  $\psi_S$ .

(iv) *UV dust attenuation.* For low- $\mu^*$  (high- $\mu^*$ ) galaxies with  $A_V = 1$ , we find typically 0.3 (1.0) mag more attenuation in the NUV compared to the C00 curve for starburst galaxies.

(v) *Emission lines.* We find that Balmer emission lines experience two to four times more attenuation than the continuum at 5500 Å within the 3-arcsec SDSS fibre aperture. The ratio of emission line to continuum dust optical depths ( $\tau_{V,\text{line}}/\tau_{V,\text{cont}}$ ) varies strongly with galaxy properties. It decreases with increasing  $\psi_S$ , increases with increasing axial ratio (decreasing inclination) and is lower in high- $\mu^*$  than in low- $\mu^*$  galaxies.

(vi) *Radial gradients.* Radial gradients are significant in all samples, and increase with increasing  $\psi_S$ . The strength of the gradients is not modified by the presence of a bulge.

### 7.1 Comparison to the two-component dust model

The primary aim of this paper is to measure the shape of the dust attenuation curve of star-forming galaxies of different types. We now provide simple qualitative arguments to interpret the observed trends in the context of the distribution of dust and stars in galaxies. Fig. 13 depicts a pictorial representation of one possible configuration for the global distribution of dust in star-forming galaxies, which can account for the majority of our results. This model for the distribution of dust relative to stars is based upon the popular two-component dust model, in which star-forming regions are surrounded by dense birth clouds, which evaporate on time-scales similar to the main-sequence lifetimes of B stars ( $\sim 10^7$  yr). The remainder of the ISM contains diffuse dust.

This two-component dust distribution has been included in several models for dust in galaxies (Silva et al. 1998; Charlot & Fall 2000; Popescu et al. 2000; Tuffs et al. 2004). However, many important details of the model are unconstrained by observations. For example, how is the diffuse dust distributed relative to stars in the galaxy discs, how does dust content change with SFRs, and what is the covering factor of the stellar birth clouds? Here, we attempt to address these questions in light of our new results combined with results in the literature.

#### 7.1.1 Covering factor of birth clouds

As discussed in detail in Section 1, one popular method for studying dust attenuation in galaxies is by comparing the SEDs of inclined and face-on galaxies. Through such a study, Yip et al. (2010) found that the distribution of the ratio of H $\alpha$  to H $\beta$  luminosity does not

<sup>10</sup> Note that this is different from Calzetti et al. (2000) who define the normalization by the amount of dust in the Balmer emission lines, and include the conversion between the amount of dust in the lines and continuum in the formula for the attenuation curve itself.

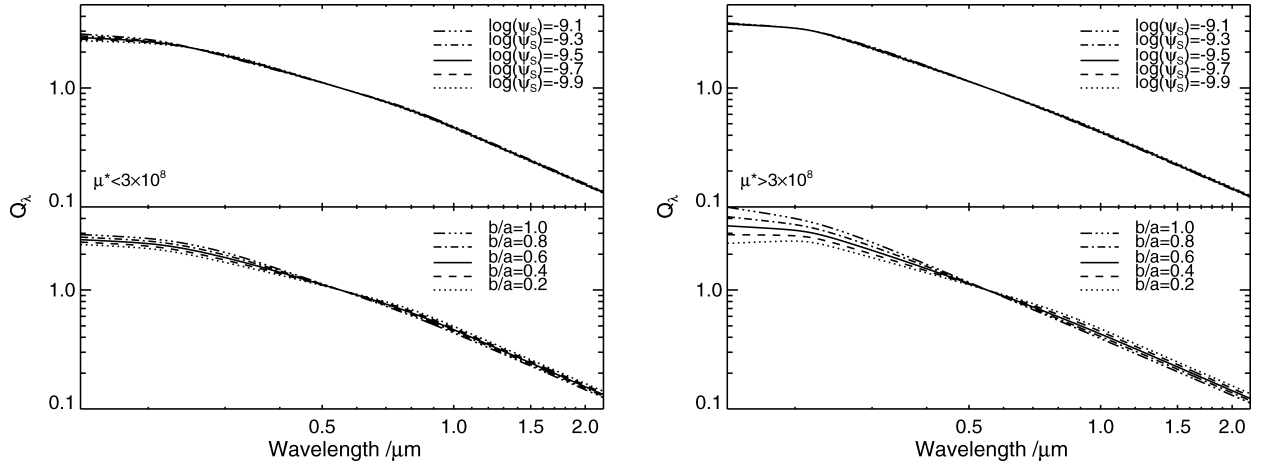


**Figure 10.** Dust attenuation curve shape ( $Q_\lambda$ ), as given by equation (18), as a function of  $\bar{\psi}_S$  (top panels) and axial ratio (bottom panels) for galaxies with low  $\mu^*$  (left-hand panels) and high  $\mu^*$  (right-hand panels). Attenuation curves at the values of  $\log_{10} \bar{\psi}_S = [-9.9, -9.7, -9.5, -9.3, -9.1]$  and  $b/a = [0.2, 0.4, 0.6, 0.8, 1.0]$  are shown as different style lines, as indicated in the top right-hand side of each panel. When variation with  $\bar{\psi}_S$  ( $b/a$ ) is shown,  $b/a$  ( $\log_{10} \bar{\psi}_S$ ) is held constant at 0.6 ( $-9.5$ ).

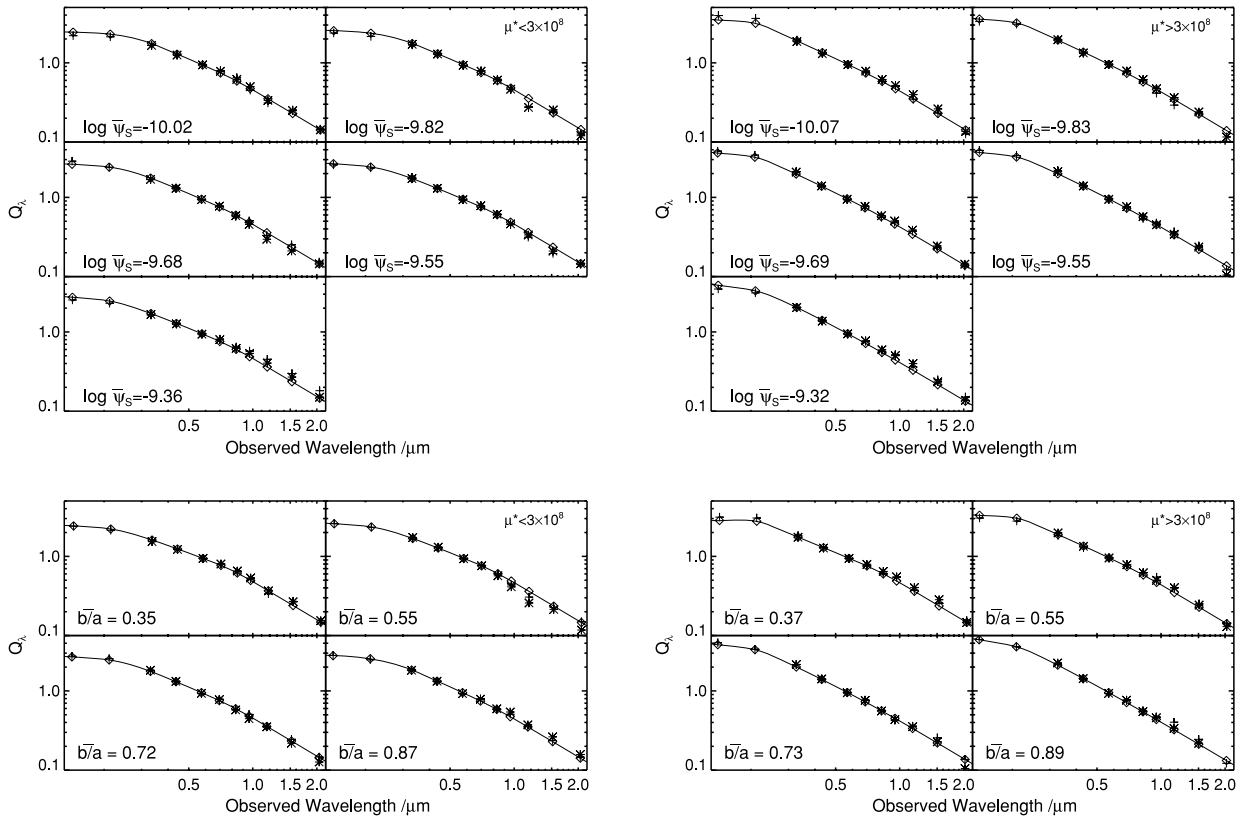


**Figure 11.** The observed shape of the dust attenuation curves in the binned samples (with UV data: crosses; without UV data: stars [i.e. normalized version of Figs 2 and 3]), compared with the empirical dust curve shapes derived from the entire (unbinned) samples (line and diamonds). The median  $\bar{\psi}_S$  and  $b/a$  of the binned samples have been used to extract the appropriate attenuation curve from equation (18); these are given at the bottom left-hand side of each panel. The left-hand (right-hand) panels show the low- $\mu^*$  (high- $\mu^*$ ) samples. The top (bottom) panels show the samples binned in  $\bar{\psi}_S$  ( $b/a$ ).

vary with galaxy inclination. There are two plausible explanations for this result: (i) emission lines are attenuated predominantly by the birth cloud from which they originate. The increase in dust opacity caused by an increase in path-length through the diffuse ISM dust is insignificant in comparison to the difference in dust opacity between the birth clouds and ISM. (ii) Sightlines to star-forming regions that lie deeper within a galaxy are entirely opaque,

causing us to measure the dust opacity only towards star-forming regions in an outer ‘skin’.

These different scenarios can alternatively be expressed in terms of the covering factor of stellar birth clouds in galaxies. If the covering factor is high, optical radiation from stars and gas produced in the inner layers of the galaxy will have near-unit probability of being absorbed by a dense cloud before escaping from the galaxy

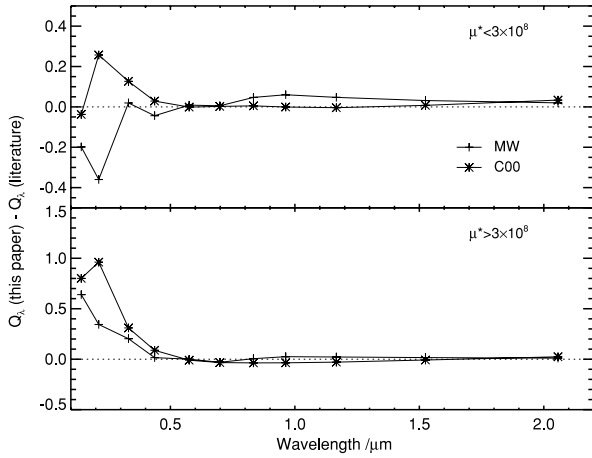


**Figure 12.** The difference between the shapes of the attenuation curve derived in this paper for galaxies with  $\log_{10}\psi_S = -9.5$  and  $b/a = 0.6$ , and the C00 (stars) and MW (crosses) curves. The top (bottom) panel shows the comparison with the attenuation curve for low- $\mu^*$  (high- $\mu^*$ ) galaxies. The NUV point on the MW curve has been convolved with the *GALEX* NUV filter for this comparison; this convolution is not necessary for other wavelengths or for the C00 curve (see Fig. 8).

(skin model). Such an effect is not supported in general by the fact that SFR estimates from optical emission lines correlate well with those estimated from mid-IR and far-IR radiation; nor by the weak trend between  $\psi_S$  and  $b/a$  mentioned in Section 4; nor by the weak trend between  $H\alpha$  equivalent width and inclination measured by Yip et al. (2010). Additional evidence against a significant skin effect comes from measurements of  $H\alpha$  rotation curves, which find less than unity optical depths to  $H\alpha$  at all but the steepest inclination angles (Goad & Roberts 1981; Giovanelli & Haynes 2002; Misiriotis 2005).

These observational results suggest that optically-thick birth clouds have a low covering factor in ordinary star-forming galaxies. Only in highly inclined galaxies do we see some evidence for a skin effect, as we observe a slight decrease in observed radial gradient strength (Fig. 6). It is well known that optical data alone are insufficient to study some unusual galaxies, due to large dust optical depths. Does this limitation of optical data apply to the general

galaxy population? Our results suggest that only in highly inclined galaxies and galaxies with very high  $\psi_S$ , where the diffuse dust optical depths are high due to long path-lengths or large diffuse dust contents, are optical data limited by dust.

### 7.1.2 Dust scaleheight and mixing with stars

If stellar birth clouds have a small covering factor, then most of the light dominating the UV–NIR emission from a star-forming galaxy has been attenuated by diffuse ISM dust alone. The geometrical arrangement of stars mixed with a dusty ISM can lead to an attenuation curve that is flatter (i.e. greyer) than the underlying extinction curve. This is because, at any wavelength, the emergent radiation is dominated by photons that are emitted by sources lying behind dust columns with less than unity optical depth. Thus, emergent red light originates from deeper within the galaxy than blue light, and attenuation appears more constant with wavelength. In Section 5.1 and Fig. 4, we found that, in contrast, galaxies with high  $\mu^*$  have an attenuation curve that is *steeper* than expected at UV–optical wavelengths. This could occur if older/redder stars suffer less attenuation on average than younger/bluer stars, for example, if both the younger stars and diffuse dust have a smaller scaleheight than older stars. In the case of high- $\mu^*$  galaxies, there could be an additional effect from the presence of a bulge: galaxy bulges tend to have older stellar populations than galaxy discs, and sightlines not obscured by the disc may have lower dust contents.

The observed universality of the slope of the NIR attenuation curve (Fig. 5), with a value equal to that of the MW extinction curve, implies a universal-size distribution for large dust grains, and additionally sets further constraints on the relative geometry of old stars and dust in galaxies. For the old stars to suffer screen-like dust extinction, they must predominantly lie outside the dust disc. This could occur through heating/migration effects of stars in galaxy discs, or through the thick disc being built through minor mergers of satellite galaxies which cease star formation as soon as they lose their gas supplies.

Xilouris et al. (1999) and Dalcanton, Yoachim & Bernstein (2004) have also suggested that diffuse interstellar dust is distributed throughout the disc with a smaller scaleheight than that of the stars, following observations of a small number of local galaxies. A variable scaleheight for dust is also included in the models of, for

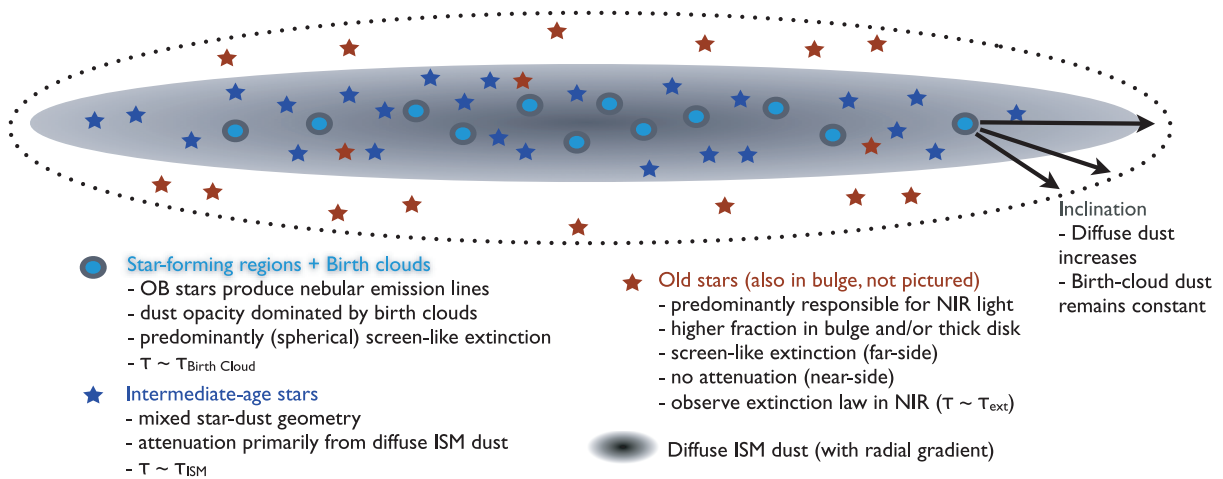


**Figure 13.** Pictorial representation of the distribution of dust in galaxies, which qualitatively can account for most results found in this paper. The bulge has been omitted for clarity, but is expected to contain predominantly old stars with little diffuse dust.

example, Tuffs et al. (2004). Matching the trends presented in this paper to detailed models of the dust and star distribution in galaxies will reveal quantitative values such as the relative scaleheights of stars and dust and the total opacity in galactic discs, as a function of specific SFR.

### 7.1.3 Diffuse and birth-cloud dust

In Section 5.4 and Fig. 7, we observe strong trends in the ratio of line-to-continuum dust opacity as a function of axial ratio,  $\psi_S$  and  $\mu^*$ . As discussed above, within the framework of the two-component dust model, the greater attenuation observed in the nebular emission lines compared to the stellar continuum is attributed to the additional attenuation caused by the stellar birth clouds surrounding the hot OB stars that produce the emission lines. The covering factor of these birth clouds is unknown, although we argued above that it is likely to be small. If this is the case, then we can, to first approximation, assume that the attenuation of the emission lines arises primarily from dust in the birth clouds, and the attenuation of the stellar continuum arises from dust in the diffuse ISM.

In more inclined galaxies, the path-length through the diffuse dust is greater: the observed opacity towards all sources lying within the dust disc increases with increasing inclination. This can have a significant effect on the optical depth measured in the continuum. By virtue of the significantly larger opacities of the birth clouds compared to the diffuse ISM dust, inclination will have less impact on the total optical depth measured in the Balmer emission lines so long as the opacity of the ISM is low enough. Thus, the observed correlation between the ratio of line to continuum dust opacity and axial ratio, and the invariance of the ratio of  $H\alpha$  to  $H\beta$  luminosity with inclination found by Yip et al. (2010), is consistent with a two-component dust model, in which the birth clouds have significantly greater dust optical depths than the diffuse ISM. The increase in strength of the 2175-Å absorption feature with inclination in the bulge-dominated galaxies may also be related to an increase in diffuse dust opacity. However, the lack of a similar trend in the low- $\mu^*$  galaxies is puzzling. The answer to this question may provide clues to the nature of the grain responsible for the 2175-Å absorption feature.

At least two factors could cause the trend found between the ratio of line to continuum dust opacity and  $\psi_S$ . First, the greater contribution of young stars to the  $V$ -band continuum light in high- $\psi_S$  galaxies may cause the measured  $\tau_{V,\text{cont}}$  to approach  $\tau_{V,\text{line}}$  at high  $\psi_S$  if these younger stars suffer greater dust attenuation relative to older stars. Secondly, a decrease in diffuse dust content from star-forming to quiescent galaxies would reproduce the observed trend. Given the significant amplitude of the observed trend, and the small quantities of diffuse dust found in elliptical galaxies, we believe this to be the most plausible explanation. Such an evolution would have implications for theories of dust grain formation during star formation, and dust grain destruction in the diffuse ISM. The larger ratio of line to continuum dust opacity in low- $\mu^*$  galaxies may relate to a decreased diffuse dust content in these lower metallicity galaxies. The trend is in qualitative agreement with observations of diffuse FIR emission, which show that later-type spirals having a lower fraction of diffuse dust than early-type spirals (Sauvage & Thuan 1992).

Finally, the strong radial gradients found in the attenuation of the stellar continua (Fig. 6) imply that the central regions of galaxies are dustier than the outskirts, a result presumably related to the metallicity gradients observed in galaxy discs. The link between  $\psi_S$

and dust content is intriguing, but observationally we are limited by the 3-arcsec SDSS fibre; spatially resolved spectroscopic studies of spiral galaxies will allow us to explore this area further.

### 7.1.4 Summary

Taken together, our observations are broadly consistent with the popular two-component model for the distribution of dust in galaxies, although several points remain unexplained. In Fig. 13, we have suggested some improvements to the basic picture, based upon results in this paper. In detail, we suggest a low covering factor for the dense birth clouds surrounding the youngest stars, we infer a scaleheight for the dust that is smaller than that of the old stars, and we suggest a radial gradient in the amount of diffuse ISM dust with more dust found towards the centre of the galaxy, particularly in galaxies with high  $\psi_S$ . Clearly, a more quantitative comparison between our results and detailed models will lead to a deeper understanding of the production and destruction of dust in the Universe.

## 7.2 Applying the dust attenuation curve

The general properties of the galaxies studied in this paper are summarized in Fig. 1, and the dust curves presented here should be applied with caution to galaxies outside these ranges. In order to apply the dust attenuation curves provided in this paper to the SED of a star-forming galaxy, we should follow the steps given below:

- (i) Does the galaxy have a significant bulge? If so, use the coefficients for the high- $\mu^*$  galaxies. Otherwise, use the coefficients for the low- $\mu^*$  galaxies.
- (ii) Determine the inclination and  $\psi_S$  of the galaxy, and if either is unknown, then set  $b/a = 0.6$  and  $\log \psi_S = -9.5$ .
- (iii) Determine  $\tau_{V,\text{cont}}$  of the galaxy. If using the Balmer emission lines, then
  - (a) take into account the strong dependence of  $\tau_{V,\text{line}}/\tau_{V,\text{cont}}$  on inclination and  $\psi_S$ ; and
  - (b) ensure that the emission lines are measured using the same aperture as the continuum data, or correct for radial gradients using Fig. 6.
- (iv) Determine the shape of the appropriate attenuation curve from equation (18), or using the IDL code provided in Appendix C.

The attenuation curves presented in this work, like that of C00, account for the effects of mixed dust–star geometry and global geometry in galaxies. Unlike the MW, or Magellanic extinction curves, our attenuation curve does not assume a screen-like dust geometry. Additionally, including the dependence on  $\psi_S$  accounts for the different forms of attenuation that different types of stars suffer from, and the changing balance of these types of star to the integrated light of the galaxy depending on the SFR of the galaxy.

## ACKNOWLEDGMENTS

The authors would like to thank the referee, M. Boquien, for his thorough reading of the text and helpful comments that improved the clarity of the text. We gratefully acknowledge David Hill and Simon Driver for their help in assessing photometric errors using GAMA comparison data; Nicholas Cross, Nigel Hambly, Paul Hewett, Simon Hodgkin, Mike Irwin and Steve Warren for their help with using the UKIDSS data set; Masataka Fukugita for useful discussions; Christy Tremonti for her initial work on the project; and Sundar Srinivasan and Gustavo Bruzual for sharing their asymptotic giant branch star expertise.

VW acknowledges support from a Marie Curie Intra-European fellowship, the visitor programme of the Institut d'astrophysique de Paris, and European Research Council Grant (PI: J. Dunlop). OV is supported by the Ministry of Science and Technological Development of the Republic of Serbia through the project no. 176021.

## REFERENCES

- Abazajian K. N. et al., 2009, *ApJS*, 182, 543  
 Baldwin J. A., Phillips M. M., Terlevich R., 1981, *PASP*, 93, 5  
 Bertoldi F., Carilli C. L., Cox P., Fan X., Strauss M. A., Beelen A., Omont A., Zylka R., 2003, *A&A*, 406, L55  
 Boissier S., Boselli A., Buat V., Donas J., Milliard B., 2004, *A&A*, 424, 465  
 Böker T. et al., 1999, *ApJS*, 124, 95  
 Boquien M. et al., 2009, *ApJ*, 706, 553  
 Bouwens R. J. et al., 2009, *ApJ*, 705, 936  
 Bouwens R. J. et al., 2010, *ApJ*, 708, L69  
 Brinchmann J., Charlot S., White S. D. M., Tremonti C., Kauffmann G., Heckman T., Brinkmann J., 2004, *MNRAS*, 351, 1151  
 Buat V., Giovannoli E., Takeuchi T. T., Heinis S., Yuan F.-T., Burgarella D., Noll S., Iglesias-Páramo J., 2011, *A&A*, 529, 22  
 Budavári T. et al., 2009, *ApJ*, 694, 1281  
 Burgarella D. et al., 2005, *ApJ*, 619, L63  
 Calzetti D., 1997a, *AJ*, 113, 162  
 Calzetti D., 1997b, in Waller W. H., Fanelli M. N., Hollis J. E., Danks A. C., eds, *AIP Conf. Proc. Vol. 408, The Ultraviolet Universe at Low and High Redshift*. Am. Inst. Phys., New York, p. 403  
 Calzetti D., 2001, *PASP*, 113, 1449  
 Calzetti D., Kinney A. L., Storchi-Bergmann T., 1994, *ApJ*, 429, 582  
 Calzetti D., Armus L., Bohlin R. C., Kinney A. L., Koornneef J., Storchi-Bergmann T., 2000, *ApJ*, 533, 682 (C00)  
 Calzetti D. et al., 2007, *ApJ*, 666, 870  
 Cardelli J. A., Clayton G. C., Mathis J. S., 1989, *ApJ*, 345, 245  
 Casali M. et al., 2007, *A&A*, 467, 777  
 Charlot S., Fall S. M., 2000, *ApJ*, 539, 718  
 Charlot S., Longhetti M., 2001, *MNRAS*, 323, 887  
 Conroy C., Schiminovich D., Blanton M. R., 2010, *ApJ*, 718, 184  
 da Cunha E., Charlot S., Elbaz D., 2008, *MNRAS*, 388, 1595  
 da Cunha E., Eminian C., Charlot S., Blaizot J., 2010, *MNRAS*, 403, 1894  
 Dalcanton J. J., Yoachim P., Bernstein R. A., 2004, *ApJ*, 608, 189  
 Draine B. T., 2003, *ARA&A*, 41, 241  
 Draine B. T., 2009, in Henning T., Grün E., Steinacker J., eds, *ASP Conf. Ser. Vol. 414, Cosmic Dust - Near and Far*. Astron. Soc. Pac., San Francisco, p. 453  
 Driver S. P., Popescu C. C., Tuffs R. J., Liske J., Graham A. W., Allen P. D., de Propriis R., 2007, *MNRAS*, 379, 1022  
 Dunlop J. S., McLure R. J., Robertson B. E., Ellis R. S., Stark D. P., Cirasuolo M., de Ravel L., 2011, *MNRAS*, submitted (arXiv:1102.5005)  
 Fukugita M., Ichikawa T., Gunn J. E., Doi M., Shimasaku K., Schneider D. P., 1996, *AJ*, 111, 1748  
 Gadotti D. A., 2009, *MNRAS*, 393, 1531  
 Gallazzi A., Charlot S., Brinchmann J., White S. D. M., Tremonti C. A., 2005, *MNRAS*, 362, 41  
 Gilbank D. G., Baldry I. K., Balogh M. L., Glazebrook K., Bower R. G., 2010, *MNRAS*, 405, 2594  
 Giovanelli R., Haynes M. P., 2002, *ApJ*, 571, L107  
 Goad J. W., Roberts M. S., 1981, *ApJ*, 250, 79  
 Gordon K. D., Calzetti D., Witt A. N., 1997, *ApJ*, 487, 625  
 Gordon K. D., Clayton G. C., Misselt K. A., Landolt A. U., Wolff M. J., 2003, *ApJ*, 594, 279  
 Granato G. L., Lacey C. G., Silva L., Bressan A., Baugh C. M., Cole S., Frenk C. S., 2000, *ApJ*, 542, 710  
 Guidorzi C. et al., 2009, *A&A*, 499, 439  
 Hambly N. C. et al., 2008, *MNRAS*, 384, 637  
 Hewett P. C., Wild V., 2007, *MNRAS*, 379, 738  
 Hewett P. C., Warren S. J., Leggett S. K., Hodgkin S. T., 2006, *MNRAS*, 367, 454  
 Hill D. T., Driver S. P., Cameron E., Cross N., Liske J., Robotham A., 2010, *MNRAS*, 404, 1215  
 Hodgkin S. T., Irwin M. J., Hewett P. C., Warren S. J., 2009, *MNRAS*, 394, 675  
 Hughes D. H. et al., 1998, *Nat*, 394, 241  
 Kauffmann G. et al., 2003a, *MNRAS*, 341, 54  
 Kauffmann G. et al., 2003b, *MNRAS*, 346, 1055  
 Kennicutt R. C., 1998, *ARA&A*, 36, 189  
 Kinney A. L., Calzetti D., Bica E., Storchi-Bergmann T., 1994, *ApJ*, 429, 172  
 Lawrence A. et al., 2007, *MNRAS*, 379, 1599  
 Maller A. H., Berlind A. A., Blanton M. R., Hogg D. W., 2009, *ApJ*, 691, 394  
 Martin D. C., Fanson J., Schiminovich D. et al., 2005, *ApJ*, 619, L1  
 Masters K. L., Giovanelli R., Haynes M. P., 2003, *AJ*, 126, 158  
 Masters K. L. et al., 2010, *MNRAS*, 404, 792  
 Mathis J. S., 1990, *ARA&A*, 28, 37  
 Ménard B., Kilbinger M., Scranton R., 2010, *MNRAS*, 406, 1815  
 Meurer G. R., Heckman T. M., Lehnert M. D., Leitherer C., Lowenthal J., 1997, *AJ*, 114, 54  
 Meurer G. R., Heckman T. M., Calzetti D., 1999, *ApJ*, 521, 64  
 Misiriotis A., 2005, *A&A*, 440, 67  
 Muñoz-Mateos J. C. et al., 2009, *ApJ*, 701, 1965  
 Noll S. et al., 2009, *A&A*, 499, 69  
 O'Donnell J. E., 1994, *ApJ*, 422, 158  
 Pei Y. C., 1992, *ApJ*, 395, 130  
 Peletier R. F., Valentijn E. A., Moorwood A. F. M., Freudling W., Knapen J. H., Beckman J. E., 1995, *A&A*, 300, L1  
 Persson C. J. L., Helou G., 1987, *ApJ*, 314, 513  
 Pierini D., Gordon K. D., Witt A. N., Madsen G. J., 2004, *ApJ*, 617, 1022  
 Popescu C. C., Misiriotis A., Kylafis N. D., Tuffs R. J., Fischera J., 2000, *A&A*, 362, 138  
 Sauvage M., Thuan T. X., 1992, *ApJ*, 396, L69  
 Schlegel D. J., Finkbeiner D. P., Davis M., 1998, *ApJ*, 500, 525  
 Schneider D. P., Gunn J. E., Hoessel J. G., 1983, *ApJ*, 264, 337  
 Silva L., Granato G. L., Bressan A., Danese L., 1998, *ApJ*, 509, 103  
 Stead J. J., Hoare M. G., 2009, *MNRAS*, 400, 731  
 Tremonti C. A. et al., 2004, *ApJ*, 613, 898  
 Tuffs R. J., Popescu C. C., Völk H. J., Kylafis N. D., Dopita M. A., 2004, *A&A*, 419, 821  
 Wild V., Hewett P. C., 2005, *MNRAS*, 361, L30  
 Wild V., Kauffmann G., Heckman T., Charlot S., Lemson G., Brinchmann J., Reichard T., Pasquali A., 2007, *MNRAS*, 381, 543  
 Wild V. et al., 2011, *MNRAS*, 410, 1593  
 Witt A. N., Gordon K. D., 2000, *ApJ*, 528, 799  
 Xilouris E. M., Byun Y. I., Kylafis N. D., Paleologou E. V., Papamastorakis J., 1999, *A&A*, 344, 868  
 Yip C.-W., Szalay A. S., Wyse R. F. G., Dobos L., Budavári T., Csabai I., 2010, *ApJ*, 709, 780

**APPENDIX A: TESTS OF THE PAIR-MATCHING METHODOLOGY**

As described in Section 2.2, there are some important features of the new pair-matching method to be aware of if the same experiment is to be repeated on different data sets. In Figs A1 and A2, we present some simple tests to show that our method is valid for the data set used in this paper.

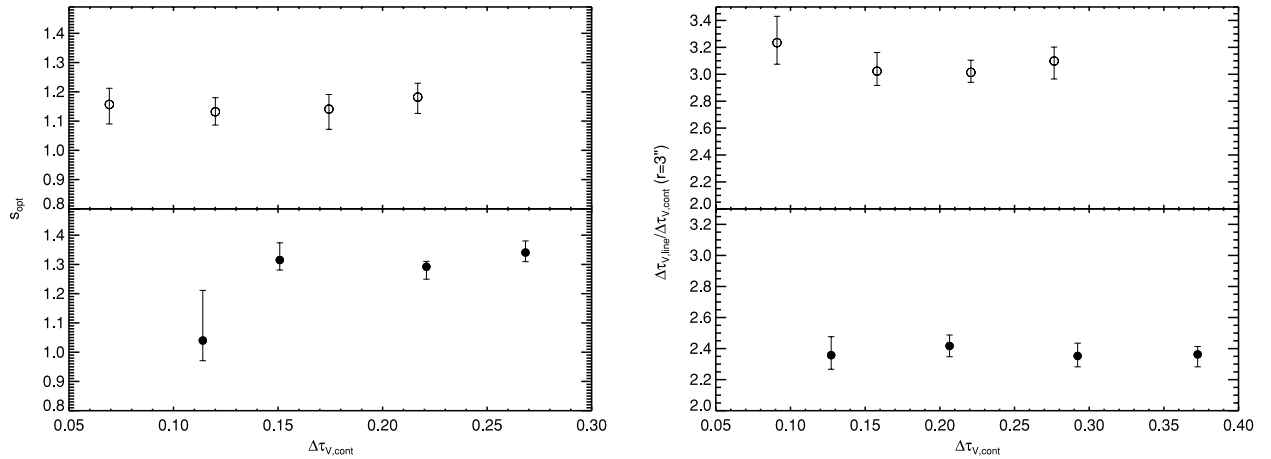


**Figure A1.** The optical slope (left-hand panels) and  $\Delta\tau_{V,\text{line}}/\Delta\tau_{V,\text{cont}}$  ratio measured from samples of low- $\mu^*$  (top panels) and high- $\mu^*$  (bottom panels) galaxies, where the pairs of galaxies are required to have  $\Delta\tau_{V,\text{line}} = [0.3, 0.5, 0.7, 0.9] \pm 0.2$  (muons from the left-hand to right-hand side). This shows that there is no variation in the shape of the dust curves or in the line-to-continuum optical depth ratio, with continuum optical depth.

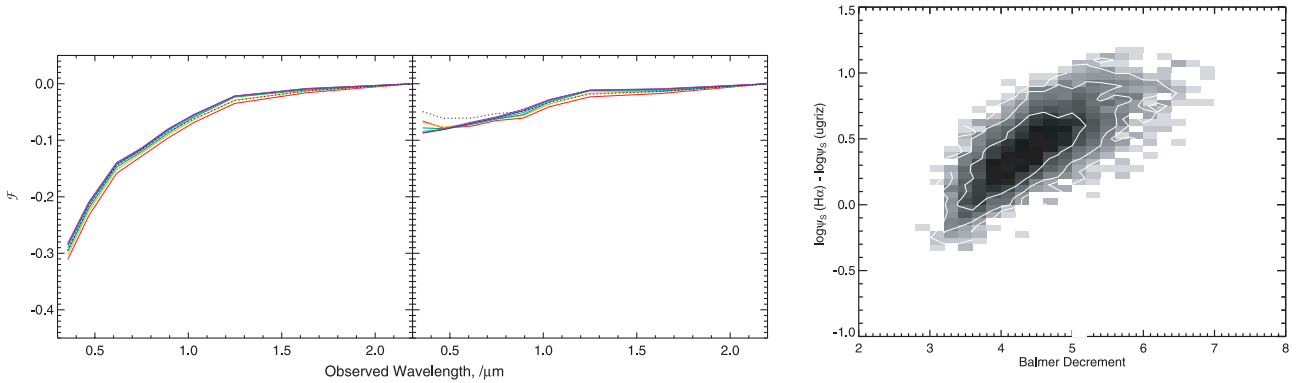


**Figure A2.** In the left-hand figure, we compare attenuation curves derived from galaxy pairs matched on  $\psi_S$  estimated from  $H\alpha$  within the 3-arcsec SDSS fibre divided by the stellar mass estimated from the optical photometry (left-hand panel), and a pure photometric estimate of  $\psi_S$  (right-hand panel). We find that the observed attenuation curves are substantially weaker when using the pair-matching based upon photometric estimates of  $\psi_S$ . In the right-hand figure, we investigate the reason for this comparing the two  $\psi_S$  estimates in the dustiest members of the pairs as a function of the ratio of  $H\alpha$  to  $H\beta$  luminosity (2D histogram in log number of galaxies). We find that the photometric  $\psi_S$  is systematically lower in galaxies with a high ratio of  $H\alpha$  to  $H\beta$  luminosity. This is not unexpected as it is difficult to distinguish dust reddening from an older stellar population using optical photometry alone. The resulting correlation between stellar population and dust content causes the attenuation curve to appear considerably flatter.

**APPENDIX B: SQL QUERIES**

The queries below are run on the SDSS Catalog Archive Server (<http://casjobs.sdss.org/casjobs/>), WFCAM Science Archive (<http://surveys.roe.ac.uk/wsa/>) and MAST Catalog Archive Server (<http://mastweb.stsci.edu/gcasjobs/>), respectively. The resulting data tables are joined manually on SDSS specObjID, using a purpose-designed IDL code. Here we provide an extract of each query; the full SQL code is available online as Supporting Information.

```

/* To obtain parameters for spectroscopic galaxies in the SDSS */

/* Basic parameters */
SELECT s.bestobjid,s.specobjid, mjd,plate,fiberid,s.z,sn_0,sn_1,
petror50_r,petror90_r,petror50_z,rowindex, p.extinction_g, p.petrorad_r,

/* Petrosian magnitudes */
p.petromag_u, p.petromag_g, p.petromag_r, p.petromag_i, p.petromag_z,

/* The number of annuli for which there is a measurable signal */
p.nprof_u, p.nprof_g, p.nprof_r, p.nprof_i, p.nprof_z,

/* The u-band AperFlux */
up0.profMean as uAperFlux0, up1.profMean as uAperFlux1,
up2.profMean as uAperFlux2, up3.profMean as uAperFlux3,
up4.profMean as uAperFlux4, up5.profMean as uAperFlux5,
up6.profMean as uAperFlux6, up7.profMean as uAperFlux7,

/* The g-band AperFlux */
gp0.profMean as gAperFlux0, gp1.profMean as gAperFlux1, [....]

/* mydb.sdssmpa_rowind contains the SDSS-MPA rowindex and specobjid for all galaxies */
FROM specobj as s, photoobjall as p, mydb.sdssmpa_rowind as m,
PhotoProfile as up0, PhotoProfile as gp0, PhotoProfile as rp0, PhotoProfile as ip0,
PhotoProfile as zp0, PhotoProfile as up1, [....]

/* Join Specobj, PhotoobjAll, SDSSMPA_rowind and select only spectroscopic galaxies */
WHERE s.specobjid=p.specobjid AND s.specobjid=m.specobjid AND s.specclass=2 AND

/* Join u-band PhotoProfiles */
s.bestobjid = up0.objid AND up0.band = 0 AND up0.bin = 0 AND
s.bestobjid = up1.objid AND up1.band = 0 AND up1.bin = 1 AND
s.bestobjid = up2.objid AND up2.band = 0 AND up2.bin = 2 AND
s.bestobjid = up3.objid AND up3.band = 0 AND up3.bin = 3 AND
s.bestobjid = up4.objid AND up4.band = 0 AND up4.bin = 4 AND
s.bestobjid = up5.objid AND up5.band = 0 AND up5.bin = 5 AND
s.bestobjid = up6.objid AND up6.band = 0 AND up6.bin = 6 AND
s.bestobjid = up7.objid AND up7.band = 0 AND up7.bin = 7 AND

/* Join g-band PhotoProfiles */
s.bestobjid = gp0.objid AND gp0.band = 1 AND gp0.bin = 0 AND
[....]

```

**/\*To obtain parameters for UKIDSS sources which are spectroscopic galaxies in the SDSS.\*/**

```

SELECT  ss.specobjid, ls.sourceid, x.distancemins,

/* Petrosian magnitudes */
ls.yPetroMag, ls.j_1PetroMag, ls.hPetroMag, ls.kPetroMag,

/* dust attenuation */
ls.aY, ls.aH, ls.aJ, ls.aK,

/* Petrosian radii */
yd.PetroRad as yPetroRad, jd.PetroRad as j_1PetroRad, hd.PetroRad as hPetroRad,
kd.PetroRad as kPetroRad,

/* UKIDSS Aper mags */
yd.Aperflux1 as yAperFlux1, jd.AperFlux1 as j_1AperFlux1, hd.AperFlux1 as hAperFlux1,
kd.AperFlux1 as kAperFlux1,
yd.Aperflux2 as yAperFlux2, [...]

/* J band exposure time */
mf.expTime

FROM lasYJHKSource AS ls, bestdr7..specobj as ss, lasSourceXDR7PhotoObj as x,
lasYJHKMergeLog AS ml, lasDetection as jd, lasdetection as hd, lasdetection as yd,
lasdetection as kd, multiframe as mf

WHERE x.masterobjid=ls.sourceid AND ss.bestobjid=x.slaveobjid AND
ls.framesetID = ml.framesetID AND ml.j_1mfID = mf.multiframeID AND

/* Join merge log to detection for the J frame: */
ml.j_1mfID = jd.multiframeID AND ml.j_1eNum = jd.extNum AND
/* Join source to detection to look up the detection required: */
ls.j_1SeqNum = jd.seqNum AND
[...]

/* remove blended objects */
ls.yppErrBits&0x00000010 = 0 AND ls.j_1ppErrBits&0x00000010 = 0 AND
ls.hppErrBits&0x00000010 = 0 AND ls.kppErrBits&0x00000010 = 0 AND

/* now get spectroscopic galaxies and select the nearest match */
ss.specclass=2 AND distanceMins<0.033333 AND
distanceMins IN ( SELECT MIN(distanceMins) FROM lasSourceXDR7PhotoObj
WHERE masterObjID=x.masterObjID AND sdssPrimary=1)

/* Basic parameters */
SELECT ss.bestobjid, ss.specobjid, gg.objid, gg.distance, gg.reversemultiplematchcount,

/* GALEX Fluxes */
ga.nuv_flux, ga.nuv_fluxerr,ga.fuv_flux, ga.fuv_fluxerr, ga.e_bv

/* myDB.dr7SFgal contains an uploaded list of all the specobjids we want to match */
FROM myDB.dr7SFgal as ss, galexgr4plus5..xsdssdr7 as gg, galexgr4plus5..photoobj as ga

WHERE ss.bestobjid=gg.SDSSobjid and gg.objid=ga.objid and gg.reversedistancerank=1

```

**APPENDIX C: IDL CODE TO COMPUTE THE DUST CURVE**

```

FUNCTION VW_DUSTCURVE, wave, flux, tau_v, flag_mustar, ssfr=ssfr,ba=ba,
      silent=silent, magnitudes=magnitudes

;+
; NAME: VW_DUSTCURVE
;
; AUTHORS:
;   Vivienne Wild <vw@roe.ac.uk>
;
; PURPOSE:
;   Calculate the unattenuated galaxy spectral energy distribution
;   followingt the prescription of Wild et al. 2011
;
; CALLING SEQUENCE:
;   unattenuated_flux = VW_DUSTCURVE(wave,flux,tau_v, flag_mustar, [ssfr=, ba=])
;
; INPUTS:
;   wave           = wavelength array in microns, not to extend beyond [0.14,2.05]
;   flux           = flux array (or magnitudes, see /magnitudes keyword)
;   tau_v          = optical depth in the stellar continuum at 5500Angstrom
;   flag_mustar    = -1 for high stellar surface mass density, or bulge-dominated
;                   = 1 for low stellar surface mass density, or disk-dominated
;
; OPTIONAL INPUTS:
;   ssfr           = logarithm of the specific star formation rate of
;                   the galaxy in years (log(psi_s/yr^-1). If none is
;                   supplied, -9.5 is assumed
;   ba             = minor/major axis ratio of galaxy. If none is
;                   supplied then 0.6 is assumed.
;
; KEYWORD PARAMETERS:
;   silent         = set to prevent some messages
;   magnitudes     = set to correct an array of magnitudes, rather than fluxes
;
; OUTPUTS:
;   unattenuated_flux = unattenuated flux array
;
; REFERENCES: [1] Wild, Charlot, Brinchmann et al., 2011, MNRAS, submitted
;
; NOTES:
;
; MODIFICATION HISTORY:
;   2011 First implementation in IDL V. Wild
;-
;*****
; Copyright (c) 2011, Vivienne Wild
;
; Permission to use, copy, modify, and/or distribute this software for any
; purpose with or without fee is hereby granted, provided that the above
; copyright notice and this permission notice appear in all copies.
;
; THE SOFTWARE IS PROVIDED "AS IS" AND THE AUTHOR DISCLAIMS ALL WARRANTIES
; WITH REGARD TO THIS SOFTWARE INCLUDING ALL IMPLIED WARRANTIES OF
; MERCHANTABILITY AND FITNESS. IN NO EVENT SHALL THE AUTHOR BE LIABLE FOR
; ANY SPECIAL, DIRECT, INDIRECT, OR CONSEQUENTIAL DAMAGES OR ANY DAMAGES
; WHATSOEVER RESULTING FROM LOSS OF USE, DATA OR PROFITS, WHETHER IN AN
; ACTION OF CONTRACT, NEGLIGENCE OR OTHER TORTIOUS ACTION, ARISING OUT OF
; OR IN CONNECTION WITH THE USE OR PERFORMANCE OF THIS SOFTWARE.
;*****

```

```

; Return to caller on error.
On_Error, 2

n = 20d ;smoothing parameter

lc_1_eff = 0.2175d ;rest-frame break points
lc_2_eff = 0.3d
lc_3_eff = 0.8d

V = 0.55 ;normalised here

;-- verify inputs
if N_params() LT 4 then begin
  print, 'syntax: VW_DUSTCURVE(wave,flux,tau_v, flag_mustar, [ssfr=, ba=])'
  return, -1
endif

;-- check for b/a and ssfr
if n_elements(ssfr) eq 0 then begin
  ssfr=-9.5
  if not(keyword_set(silent)) then print, 'Assuming log(psi_s)=-9.5'
endif
if n_elements(ba) eq 0 then begin
  ba = 0.6
  if not(keyword_set(silent)) then print, 'Assuming b/a=0.6'
endif

;-- define parameters for high / low mustar cases
if flag_mustar eq -1 then P = [1.3, 0.6, 0.1, 1.1, 0.3, -0.2, 0.2, 0.9,0.1] $
else if flag_mustar eq 1 then P = [1.1, 0.4, -0.1, 0.7, 0., 0.4, 0.15, 0.,0.2] $
else begin
  print, 'Please specify: flag_mustar = -1 for high stellar surface mass density'
  print, ' = 1 for low stellar surface mass density'
  print, 'syntax: VW_DUSTCURVE(wave,flux,tau_v, flag_mustar, [ssfr=, ba=])'
  return, -1
endif

;-- check parameters are within specified limits
ind = where(wave lt 0.14 or wave gt 2.05)
if ind[0] ne -1 then begin
  print, 'Dust curve only valid in wavelength range 0.14-2.05microns'
  return, -1
endif

if ba lt 0.3 or ba gt 0.9 then begin
  print, 'Dust curve only valid in axis ratio range 0.3-0.9, see Section 6 of [1]'
  return, -1
endif

if flag_mustar eq -1 then begin ;high mustar
  if ssfr lt -10.2 or ssfr gt -9.3 then begin
    print, 'For bulge-dominated galaxies dust curve only valid in ssfr range -10.2 -> -9.3'
    return, -1
  endif
endif

if flag_mustar eq 1 then begin ;low mustar
  if ssfr lt -10.0 or ssfr gt -9.1 then begin
    print, 'For disk-dominated galaxies dust curve only valid in ssfr range -10.0 -> -9.1'
    return, -1
  endif
endif

```

```

;;-----
;;-- define relations with SSFR and b/a

ba_c = ba - 0.6
ssfr_c = ssfr + 9.5

;; sopt
sopt = P[0]+ba_c*P[1]+ssfr_c*P[2]

;; snir
snir = 1.6

;; snuv
snuv = P[3]+ba_c*P[4]+ssfr_c*P[5]

;; sfuv
sfuv = P[6]+ba_c*P[7]+ssfr_c*P[8]

lc_1 = lc_1_eff
lc_2 = ((lc_1^snuv)/(lc_2_eff^(snuv-sopt)))^(1/sopt)
lc_3 = ((lc_2^sopt)/(lc_3_eff^(sopt-snir)))^(1/snir)

norm = (((V/lc_1)^(sfuv*n)+(V/lc_1)^(snuv*n)+(V/lc_2)^(sopt*n)+$
        (V/lc_3)^(snir*n))^(-1/n)) ;Qlambda=1 at V

Q_lambda = (((wave/lc_1)^(sfuv*n)+(wave/lc_1)^(snuv*n)+(wave/lc_2)^(sopt*n)+$
            (wave/lc_3)^(snir*n))^(-1/n)) / norm ;eq. 18

tau_lambda = Q_lambda*tau_V

if not(keyword_set(magnitudes)) then return, flux/exp(-tau_lambda) $ ;e.g. eq 5
else return, flux - 1.086*tau_lambda ;eqn. 3

END

```

## SUPPORTING INFORMATION

Additional Supporting Information may be found in the online version of this article:

**Table 2.** Averaged attenuation curves, normalized to zero at  $K$  ( $T_\lambda$ , equation 7), for each sample studied in this paper.

**Appendix B.** Full SQL code to query the SDSS, UKIDSS and GALEX data bases.

Please note: Wiley-Blackwell are not responsible for the content or functionality of any supporting materials supplied by the authors. Any queries (other than missing material) should be directed to the corresponding author for the article.

This paper has been typeset from a  $\text{\TeX}/\text{\LaTeX}$  file prepared by the author.